Master Thesis

Performance evaluation of 50-cm PMTs for calibration of the Hyper-Kamiokande detector (ハイパーカミオカンデ検出器較正のための50cm径PMTの性能評価)

March 14, 2024

Department of Physics, Graduate School of Science
The University of Tokyo
東京大学大学院理学系研究科物理学専攻

Eiichiro Watanabe
渡辺英一朗

Abstract

Hyper-Kamiokande is the next-generation experiment that aims to measure the leptonic CP violation, determine neutrino mass ordering, observe astrophysical neutrinos, and search for proton decay. Hyper-Kamiokande, scheduled to start operation in 2027, will have approximately 20,000 newly developed 50-cm photomultiplier tubes (PMTs). Hyper-Kamiokande requires high-precision calibration to reduce systematic errors. In order to calibrate the Hyper-Kamiokande detector, it is necessary to understand the PMTs' response and establish a method to evaluate their performance before the installation. This pre-calibration is performed in air at room temperature, while the actual operation of the 50-cm PMT is in water at around 13 °C. Therefore, it is necessary to evaluate the effect of these differences in the environment around the PMT on the performance of the PMT in advance. We made the first underwater measurement of the temperature dependence of gain, relative quantum efficiency (QE), and dark rate of the 50-cm PMT for the Hyper-Kamiokande experiment. In the temperature range of 13 to 23 °C, we found that both gain and relative QE remained constant with an accuracy of $\pm 1\%$, and the dark rate variation was within 5%. In addition, a comparison of gain in air and water was made. These results provide an important guideline for the pre-calibration measurement for the Hyper-Kamiokande experiment.

Contents

Chapter 1

Physics Background

The Super-Kamiokande (Super-K, SK) [1], which began observations in 1996, has been studying neutrinos and nucleon decay. The discovery of atmospheric neutrino oscillations by the Super-Kamiokande experiment in 1998 [2] revealed that neutrinos have mass and was the evidence of the physics beyond the Standard Model. However, there are still many unresolved questions on neutrinos and proton decay has not been observed yet. The Hyper-Kamiokande (Hyper-K, HK) [3] experiment is a newly launched next-generation project which aims to answer these questions.

This chapter begins with an explanation of neutrinos, followed by some neutrino measurements that can be significantly improved at Hyper-K thanks to its large data set.

1.1 Neutrino

In the Standard Model of particle physics, neutrinos are a type of elementary particle that have no electric charge and interact with other particles only through weak interactions and gravitational interactions. Neutrinos are massless and come in three flavors, ν_e, ν_μ and ν_τ. Neutrinos were first proposed by W. Pauli in 1930 as unknown neutral particles to explain the missing energy of beta decay. The existence of neutrinos was then established experimentally in 1954 when C. Cowan and F. Reines succeeded in directly detecting electron-antineutrino from a nuclear reactor using a 300-liter liquid scintillator [4]. Although neutrinos had been considered massless particles in the Standard Model, the discovery of neutrino oscillations by the Super-K in 1998 suggested that neutrinos have a finite mass, suggesting the existence of a new theory beyond the Standard Model.

1.2 Neutrino Oscillation

Neutrinos are known to have three flavor eigenstates and they take on these eigenstates during reactions due to weak interactions. On the other hand, mass eigenstates are different from flavor eigenstates, and the flavor eigenstates $|\nu_\alpha\rangle$ ($\alpha = e, \mu, \tau$) are expressed using the mass eigenstates $|\nu_i\rangle$ ($i = 1, 2, 3$) and the

Pontecorvo-Maki-Nakagawa-Sakata (PMNS) matrix as follows.

$$|\nu_\alpha\rangle = \sum_{i=0} U_{\alpha i} |\nu_i\rangle \qquad (1.1)$$

The PMNS matrix U is a 3 × 3 unitary matrix, represented by the three mixing angles θ_{12} , θ_{13} , θ_{23} and the CP phase in the lepton sector δ_{CP} as follows.

$$U = \begin{pmatrix} 1 & 0 & 0 \\ 0 & \cos\theta_{23} & \sin\theta_{23} \\ 0 & -\sin\theta_{23} & \cos\theta_{23} \end{pmatrix} \begin{pmatrix} \cos\theta_{13} & 0 & \sin\theta_{13}e^{-i\delta_{CP}} \\ 0 & 1 & 0 \\ -\sin\theta_{13}e^{i\delta_{CP}} & 0 & \cos\theta_{13} \end{pmatrix} \begin{pmatrix} \cos\theta_{12} & \sin\theta_{12} & 0 \\ -\sin\theta_{12} & \cos\theta_{12} & 0 \\ 0 & 0 & 1 \end{pmatrix}$$
$$(1.2)$$

In the Standard Model framework, only two mass-squared differences are independent. Here, the mass-squared difference is defined as $\Delta m_{ij}^2 \equiv m_i^2 - m_j^2$. For a given energy E and baseline L, the neutrino oscillation probability ($\nu_\alpha \to \nu_\beta$) in vacuum is expressed as follows.

$$P_{(\nu_\alpha \to \nu_\beta)} = \delta_{\alpha\beta} - 4\sum_{i<j} \mathrm{Re}[U_{\alpha i} U_{\beta i}^\dagger U_{\alpha j} U_{\beta j}^\dagger] \sin^2\left(\frac{\Delta m_{ij}^2}{4E}L\right)$$
$$+ 2\sum_{i<j} \mathrm{Im}[U_{\alpha i} U_{\beta i}^\dagger U_{\alpha j} U_{\beta j}^\dagger] \sin\left(\frac{\Delta m_{ij}^2}{2E}L\right) \qquad (1.3)$$

Similarly, the oscillation probability of the antineutrino is

$$P_{(\bar\nu_\alpha \to \bar\nu_\beta)} = \delta_{\alpha\beta} - 4\sum_{i<j} \mathrm{Re}[U_{\alpha i} U_{\beta i}^\dagger U_{\alpha j} U_{\beta j}^\dagger] \sin^2\left(\frac{\Delta m_{ij}^2}{4E}L\right)$$
$$- 2\sum_{i<j} \mathrm{Im}[U_{\alpha i} U_{\beta i}^\dagger U_{\alpha j} U_{\beta j}^\dagger] \sin\left(\frac{\Delta m_{ij}^2}{2E}L\right). \qquad (1.4)$$

Neutrino oscillations can be explained by the following six parameters; three mixing angles (θ_{12},θ_{23},θ_{13}), one CP phase (δ_{CP}), and two mass squared differences. Measurements of these mixing parameters have been performed using multiple neutrino sources over a wide range of energies. θ_{12} and Δm_{21}^2 have been measured by solar and reactor neutrino experiments, and θ_{13} has been measured by experiments of reactor neutrino and accelerator neutrino which are artificially generated neutrinos by the decay of hadrons using an accelerator. θ_{23} and δm_{32}^2 have been measured by atmospheric neutrino and accelerator neutrino experiments. Among these six parameters, δ_{CP} is the only parameter whose finite value is not discovered yet.

1.2.1 Neutrino Mass Ordering

With the discovery of neutrino oscillations, neutrinos are known to have masses and their mass-squared difference has been measured. In contrast, the order of the masses of the three types of neutrinos has not yet been clarified (the mass

ordering). The case $m1 < m2 \ll m3$ is called normal ordering, and the case $m3 \ll m1 < m2$ is called inverted ordering.

The matter effect (the Mikheyev–Smirnov–Wolfenstein effect, MSW effect [5, 6]) can be used to determine mass hierarchy. Neutrinos may interact with matter in flight, but the electrons in matter cause reactions that only electron neutrinos undergo. The effect of the enhanced or suppressed oscillation probability due to the different interactions of the three types of neutrinos is called the matter effect. Thus, in principle, if the matter effect is sufficiently large, the mass ordering can be determined by measuring the oscillation probability.

1.2.2 CP Violation

The charge-parity (CP) violation can be measured by the difference of neutrino oscillation probabilities between neutrino and anti-neutrino. Using Equation 1.3 and 1.4, the difference of oscillation probabilities between neutrino and anti-neutrino can be expressed as follows;

$$
\begin{aligned}
\Delta P_{\alpha \to \beta} &= P_{(\nu_\alpha \to \nu_\beta)} - P_{(\bar{\nu}_\alpha \to \bar{\nu}_\beta)} \\
&= 4 \sum_{i<j} \mathrm{Im}[U_{\alpha i} U_{\beta i}^\dagger U_{\alpha j} U_{\beta j}^\dagger] \sin\left(\frac{\Delta m_{ij}^2}{2E} L\right).
\end{aligned} \tag{1.5}
$$

Considering the case of $\nu_\mu \to \nu_e$ and $\bar{\nu}_\mu \to \bar{\nu}_e$, Equation 1.5 can be expressed as follows;

$$
\begin{aligned}
\Delta P_{\mu \to e} &= P_{(\nu_\mu \to \nu_e)} - P_{(\bar{\nu}_\mu \to \bar{\nu}_e)} \\
&= -2 \cos\theta_{13} \sin(2\theta_{12}) \sin(2\theta_{23}) \sin(2\theta_{13}) \sin\delta_{CP} \\
&\quad \times \sin\left(\frac{\Delta m_{32}^2 L}{4E}\right) \sin\left(\frac{\Delta m_{21}^2 L}{4E}\right) \sin\left(\frac{\Delta m_{31}^2 L}{4E}\right).
\end{aligned} \tag{1.6}
$$

δ_{CP} is currently studied by long baseline neutrino experiments such as the T2K experiment, but its finite value is not observed yet. In the T2K experiment, neutrino beams (ν_μ, $\bar{\nu}_\mu$) generated at Japan Proton Accelerator Research Complex (J-PARC) in Tokai-mura are observed at the Super-K detector, 295 km away. The T2K experiment measures the asymmetry of the $\nu_\mu \to \nu_e$ oscillation probability using ν_μ and $\bar{\nu}_\mu$ beams. The effect of δ_{CP} shows up as a difference in the electron neutrino appearance probability (Fig. 1.1)and can be measured by using the reconstructed energy distribution (Fig. 1.2).
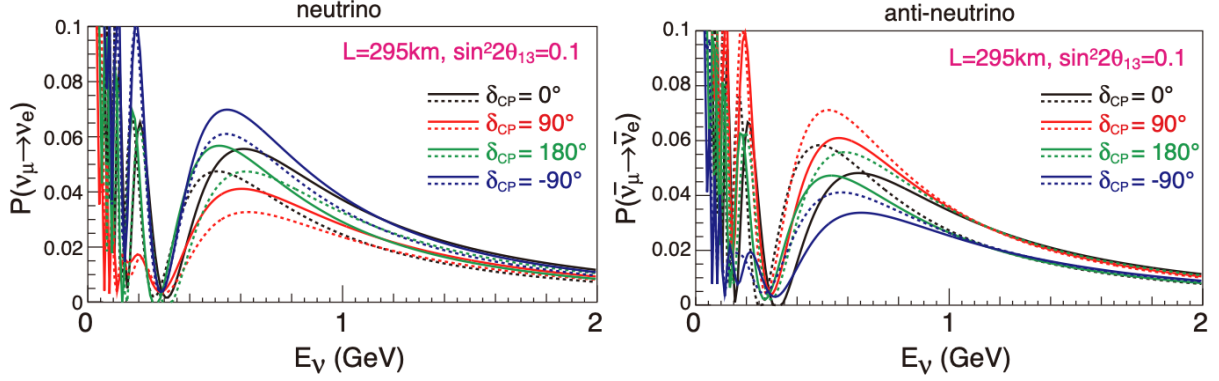
Figure 1.1. Oscillation probabilities as a function of the neutrino energy for $\nu_\mu \to \nu_e$ (left) and $\bar{\nu}_\mu \to \bar{\nu}_e$ (right) with L=295 km and $\sin^2 2\theta_{23} = 0.1$. Black, red, green, and blue lines correspond to $\delta_{CP}=$ 0°, 90°, 180° and 270°, respectively. Solid (dashed) line represents the case for a normal (inverted) mass ordering [7].
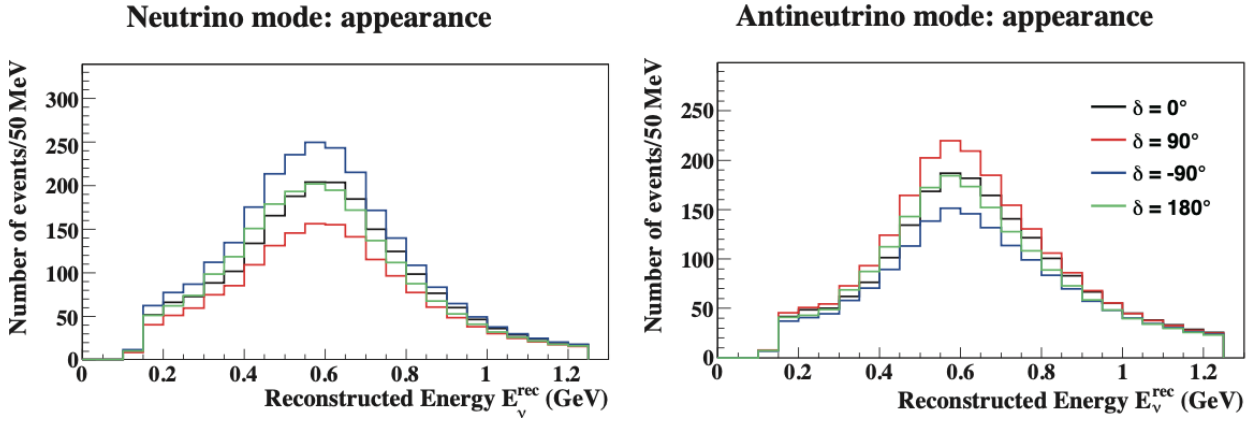

Figure 1.2. Reconstructed neutrino energy distribution for several δ_{CP} with $\sin^2 2\theta_{13} = 0.1$ and normal ordering [7].

The current best fit values of neutrino data are summarized in Table 1.1, and the latest δ_{CP} measurement results are shown in Figure 1.3. The CP-conserving values $\delta_{CP} = 0, \pi$ are excluded at 90% confidence level.

Table 1.1. Neutrino oscillation parameters. NO (IO) is normal mass ordering (inverted mass ordering) [8].

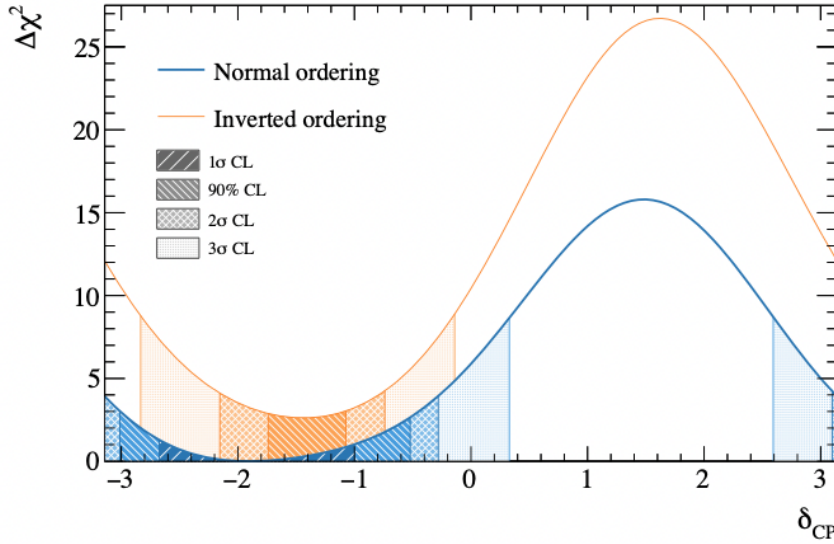| Oscillation parameter	Best fit value
$\sin^2\theta_{12}$	0.307 ± 0.013
$\sin^2\theta_{23}$ (NO)	0.546 ± 0.021
$\sin^2\theta_{23}$ (IO)	0.539 ± 0.022
$\sin^2\theta_{13}$	$(2.20 \pm 0.07) \times 10^{-2}$
Δm^2_{21}	$(7.53 \pm 0.18) \times 10^{-5}$ eV^2
Δm^2_{32} (NO)	$(2.453 \pm 0.033) \times 10^{-3}$ eV^2
Δm^2_{32} (IO)	$(\text{-}2.536 \pm 0.034) \times 10^{-3}$ eV^2

Figure 1.3. The latest δ_{CP} measurement results from T2K [9].

1.3 Solar Neutrino

Solar neutrinos are electron neutrinos produced by thermonuclear fusion reactions near the center of the Sun. The flux and spectrum of solar neutrinos are sensitive to θ_{12} and Δm^2_{21}. In addition, since neutrinos rarely interact with matter and are emitted from the center of the Sun, solar neutrino observations allow us to monitor the current state of the solar center.

Solar neutrinos are subject to the matter effect due to the high density of the solar interior and most of the electron neutrinos change to ν_μ or ν_τ. When flavor-changed solar neutrinos (ν_μ and ν_τ) pass through the Earth's interior, some of them revert back to electron neutrinos due to the Earth's matter effect. As a result, day-night asymmetry occurs in the fraction of electron neutrinos. Figure 1.4 shows the
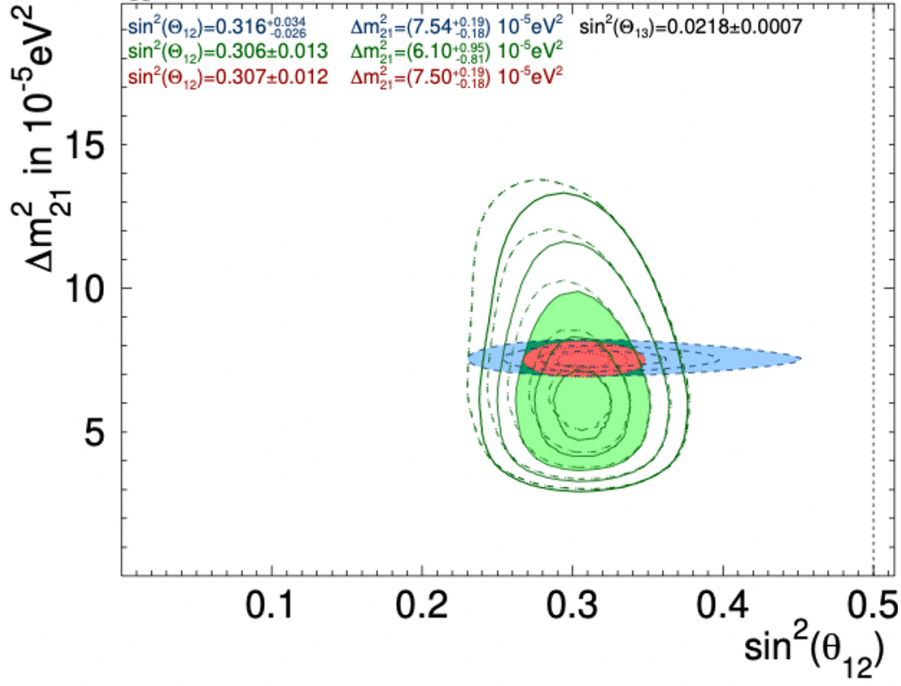
Figure 1.4. Allowed region of neutrino oscillation parameters $(\theta_{12}, \Delta m_{12}^2)$. The green area comes from the solar neutrino experiments, the blue area from the KamLAND experiments, the red from combined of two. The filled area is 3σ area [10].

latest combined results of the allowed region of neutrino oscillation parameters, θ_{12} and Δm_{12}^2 from all the solar neutrino experiments and KamLAND's reactor neutrino measurement [10]. While the mixing angle θ_{12} is consistent between solar neutrinos and reactor antineutrinos, there is 1.5σ tension in Δm_{12}^2. In this results, a non-zero day-night asymmetry was observed at a 3.1σ significance (Figure 1.4).
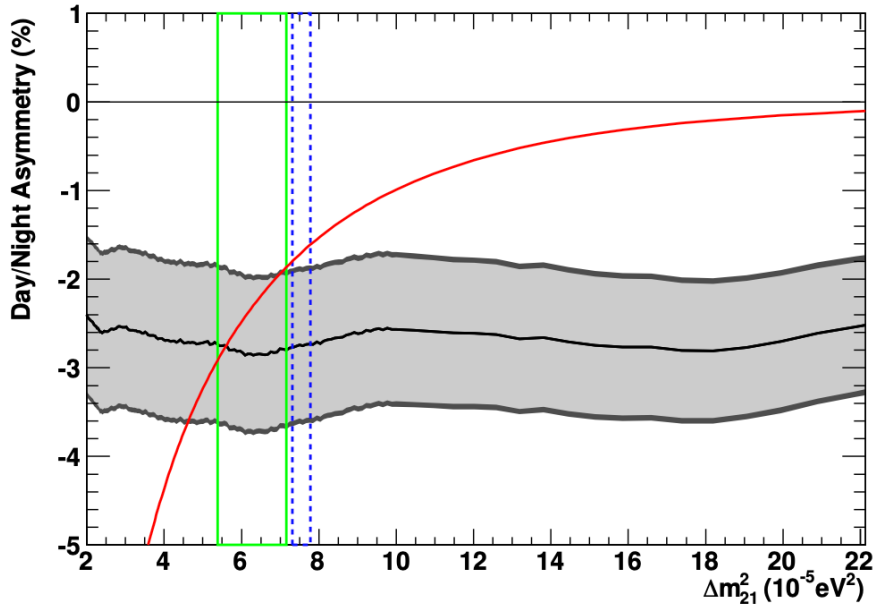
Figure 1.5. The black line (grey band) shows the best-fit value of day-night asymmetry (its uncertainty). The red curve shows the expected day-night asymmetry. The green solid (blue dashed) box shows the 1σ range allowed by solar experiments (solar experiments and KamLAND) [10].

Chapter 2

Hyper Kamiokande Experiment

The Hyper-Kamiokande detector is the successor of the Super-Kamiokande detector. This is a large water Cherenkov detector that uses 260,000 tons of ultrapure water and approximately 20,000 50 cm diameter photomultiplier tubes (PMTs) to detect Cherenkov light in water. Its construction began in 2020 at Kamioka-cho, Hida City, Gifu Prefecture, Japan, with the aim of starting operations in 2027. Using its large fiducial volume and improved photodetector, the Hyper-Kamiokande experiment aims to observe astrophysical neutrinos, including solar neutrino, measure the leptonic CP violation, and search for proton decay. This chapter provides an overview of the Hyper-Kamiokande experiment.

2.1 Water tank

The water tank of the Hyper-Kamiokande detector is a stainless steel cylindrical tank with a diameter of 68 m, a height of 71 m, and a fiducial volume of approximately 200 ktons. Figure 2.1 shows a schematic view of the Hyper-Kamiokande water tank.
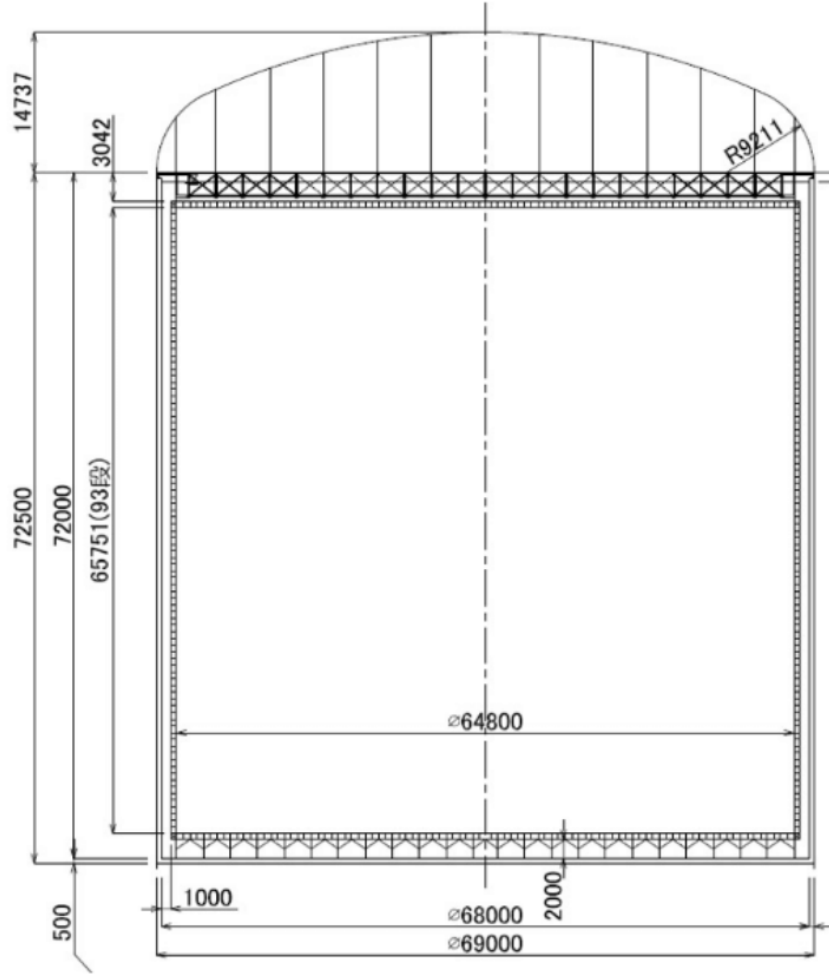
Figure 2.1. Schematic view of the Hyper-K tank [11].

The tank is divided into two main layers (Figure 2.2): the Inner Detector (ID) and the Outer Detector (OD). The ID is the main detector, which detects neutrino events and proton decay events etc. Approximately 20,000 newly developed 50 cm diameter photomultiplier tubes (HK-PMT, R12860) will be installed on the inner side of the ID, with a photocathode coverage in the ID wall of 20%. Details on this R12860 are discussed in Chapter 3. The OD is placed around the ID, with a water thickness of 1 m at the sides and 2 m at the top and bottom. The OD will be viewed by 3-inch PMTs facing outward on the outer wall of the ID. Each 3-inch PMT will be mounted on wavelength shifting plate to increase coverage and collection efficiency. OD will act mainly as a veto of incoming particles such as cosmic ray muons.
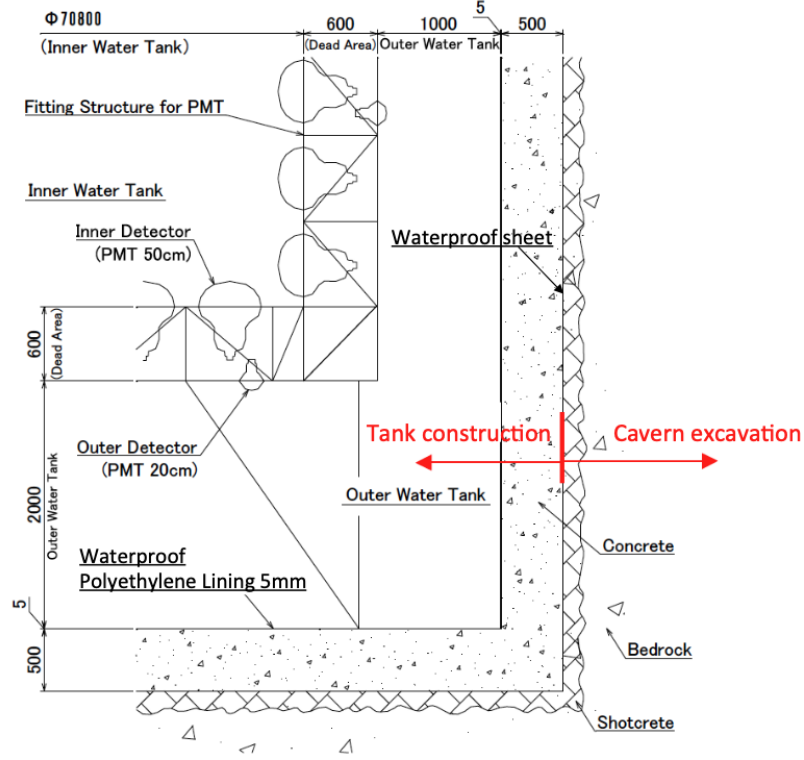
Figure 2.2. Boundary between ID and OD [7].

2.2 Particle Detection

The Hyper-K detector observes neutrinos by detecting the Cherenkov light emitted by charged particles produced by neutrino interactions with electrons and nuclei in water molecules.

2.2.1 Cherenkov Radiation

Cherenkov radiation is a phenomenon in which charged particles emit light in matter. When a high-speed charged particle travels faster than the phase velocity of light in the medium, light called Cherenkov radiation is emitted. Figure 2.3 shows the Cherenkov radiation, which is emitted in the form of a cone.
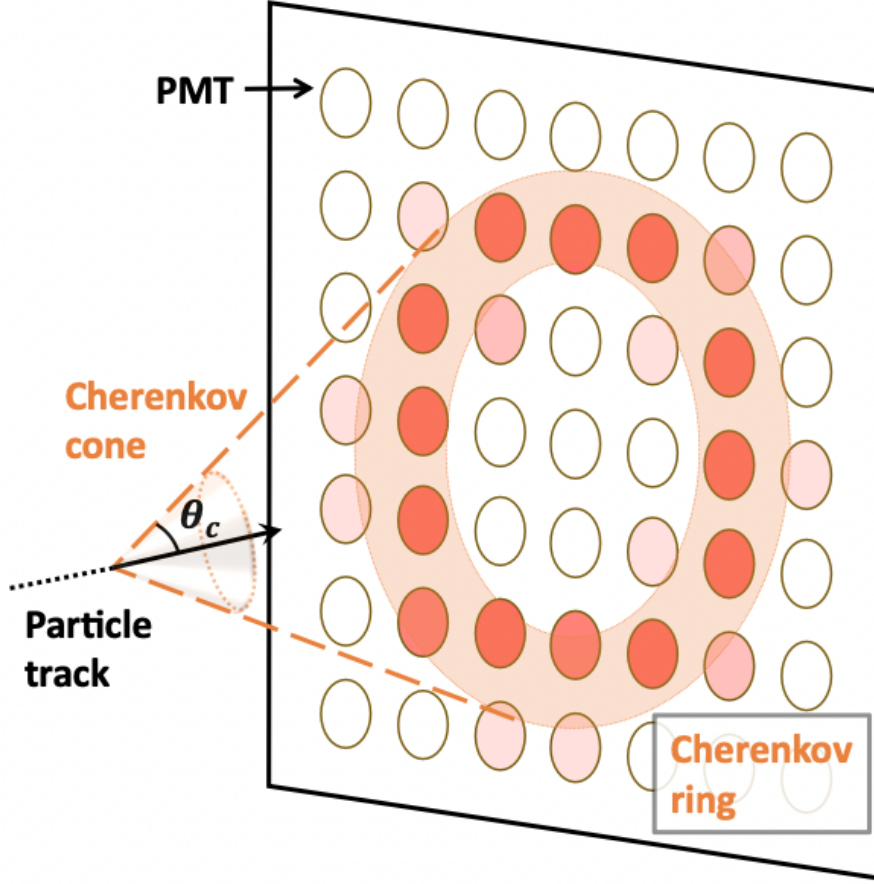
Figure 2.3. Cherenkov light radiation [12].

The opening angle of the cone, θ, is determined by the velocity of the parent particle. The relation between velocity of the charged particle $\beta(= v/c)$ and radiation angle θ is as follows,

$$cos\theta = \frac{1}{\beta n},$$
(2.1)

where n is the refractive index of the medium.

The number of Cherenkov photons emitted by a particle of charge Ze at wavelengths λ to $\lambda + d\lambda$ per unit length $dN(\lambda)$ is expressed as follows.

$$dN(\lambda) = \frac{2\pi Z^2}{137} \left\{ 1 - \left(\frac{1}{\beta n(\lambda)} \right)^2 \right\} \frac{d\lambda}{\lambda^2}$$
(2.2)

2.2.2 Cherenkov Light Observation

The Hyper-K detector can detect gamma rays and relativistic charged particles by observing the Cherenkov light described above. At the same time, it can also identify the energy, reaction position, and type of particles.

Charged particles emit photons according to the Equation 2.2 per unit length, and the light intensity increases with the range of particle. Since the range of a particle depends on the particle's energy, the energy of the particle can be reconstructed based on the light intensity distribution of the Cherenkov light. In the Hyper-K, the collected light intensity is about 5 p.e./MeV, and events below a few tens of MeV, where the averaged light intensity per PMT is much smaller than 1 p.e., are called "low-energy" events. The reaction position can be reconstructed primarily from the time distribution of photon detection. For higher energy neutrinos above a few hundred MeV, particle types can be identified from the spatial distribution of Cherenkov light. Figure 2.4 shows an example of the spatial distribution of Cherenkov light. For example, electrons and gamma-rays form an electromagnetic shower in water due to the cascade of secondary particles caused by bremsstrahlung and electron pair production. Since Cherenkov radiation is emitted from each electron and positron in the shower, the Cherenkov rings from each electron in the shower overlap, and a ring pattern with blurred contours is observed. Muons, on the other hand, do not form a shower, resulting in the observation of clearly outlined Cherenkov rings.
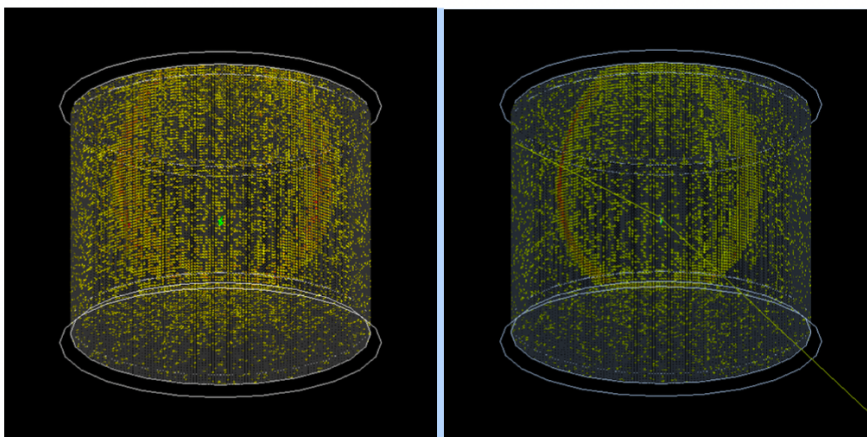

Figure 2.4. Spatial distribution of Cherenkov light, 1 GeV electron (left) and a 1 GeV muon (right) [7].

2.3 Physics goals

In this section, we describe the physics goals of Hyper-K, based on the examples of CP violation (see 1.2.2) and day-night asymmetry (see 1.3) in Chapter 1.

For δ_{CP} measurement, the T2K experiment will be succeeded by Hyper-K. Hyper-K aims to discover the CP violation in the lepton sector. Figure 2.5 shows the sensitivity to exclude δ_{CP}=0. If δ_{CP} is -π/2, the CP-conserving δ_{CP}=0 is excluded at 5σ confidence level within four years.
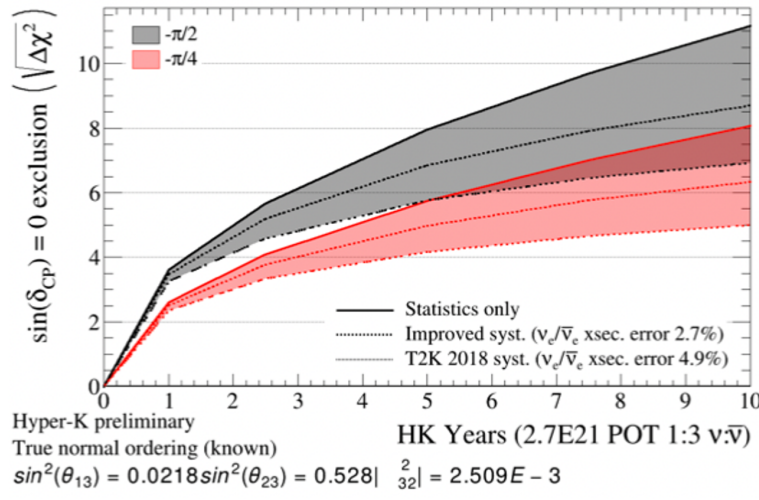
Figure 2.5. Sensitivity to exclude $\sin(\delta_{CP})$=0 for true δ_{CP}=-$\pi/2$ and -$\pi/4$, as a function of HK-years. The shaded areas indicate the range of values that can be taken when the systematic error model is varied [13].

A precise measurement of δ_{CP} is also a major goal of the Hyper-K experiment after its discovery. In this measurement, the energy scale uncertainty and the change in δ_{CP} are degenerate. Figure 2.6 shows that a shift in the energy scale and a shift in δ_{CP} have a similar effect on the electron neutrino energy spectra.
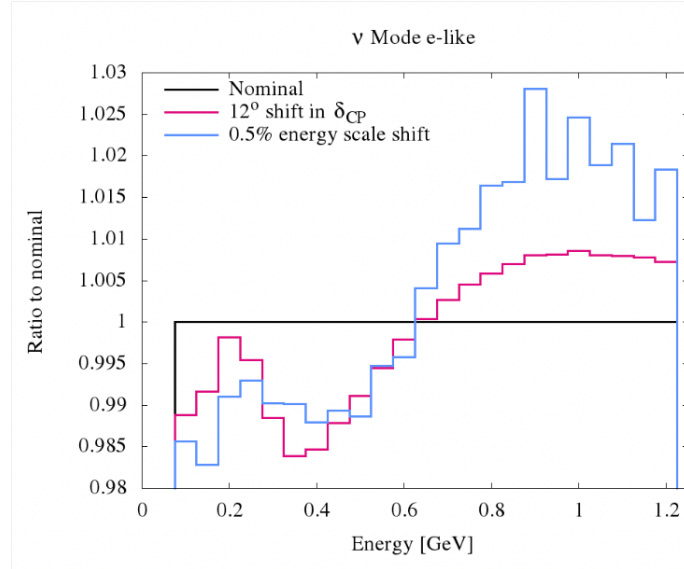
Figure 2.6. Ratio of energy spectrum predicted with δ_{CP} =-78° (magenta) and δ_{CP} =-90°, and the ratio to nominal with a 0.5% energy scale shift (blue) applied to reconstructed electron neutrino candidates [14].

Figure 2.7 shows the δ_{CP} resolution assuming different energy scale uncertainties with 10 years of Hyper-K data taking. The resolution on δ_{CP} is improved by

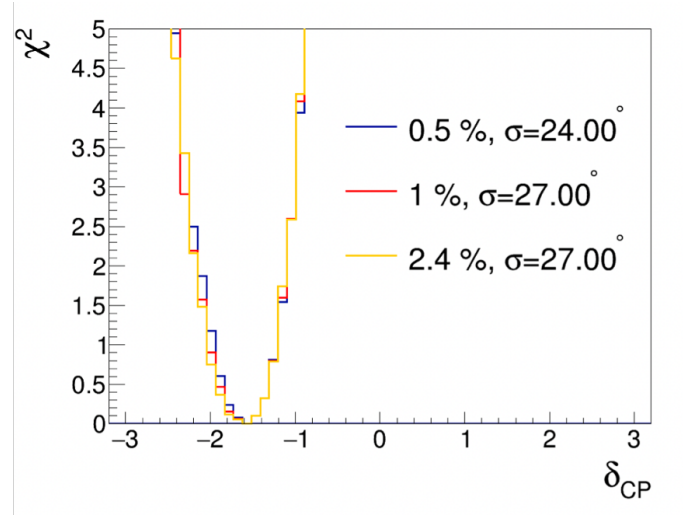reducing the energy scale uncertainty to 0.5%.

Figure 2.7. δ_{CP} 1σ contours near δ_{CP} =-$\pi/2$, assuming different energy scale uncertainties. The percentage in the legend corresponds to the energy scale uncertainty, and σ is the resolution on δ_{CP} [14].

For day-night asymmetry measurement, the Hyper-K experiment is trying to verify this day-night asymmetry with more than 4σ accuracy, and to achieve this, it is required to measure this with a systematic error of better than 0.3% (while the Super-K with 1.1% static error $\pm$ 0.5% systematic error). Figure 2.8 shows the day-night asymmetry observation sensitivity as a function of HK-years.
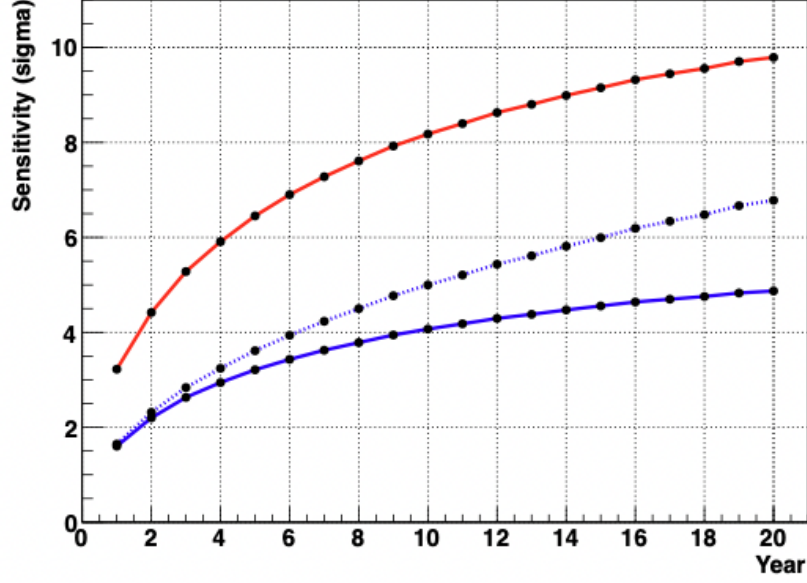
Figure 2.8. Day-night asymmetry observation sensitivity as a function of HK-years. The red line shows the sensitivity from the no asymmetry, while the blue line shows from the sensitivity to separate from the asymmetry expected by the reactor neutrino oscillation. The solid line shows the systematic uncertainty is 0.3% case, while the dotted line shows the 0.1% case [15].

2.4   Necessity of precise calibration

The larger the detector, the more high-statistical data can be obtained, but at the same time, the evaluation of systematic errors becomes more important for the physics sensitivity. The Hyper-K detector will be much larger than the Super-K detector, so the Hyper-K experiment requires much better detector systematics than the Super-K experiment.

To achieve the required systematics described in 2.3, we need to calibrate all potential systematic error sources in PMTs, electronics, and water with much better than 1% accuracy. At the same time, it is necessary to investigate the impact of systematic errors in each PMT performance on systematic errors in the energy scale and fiducial volume.

Chapter 3

50cm-PMTs for Hyper-Kamiokande

The Hyper-K detector requires photosensors with higher performance than Super-K. The minimum requirements for the Hyper-K photosensors are listed in Table 3.1. Among many candidates, the R12860 50 cm Box & Line (B&L) PMT from Hamamatsu Photonics K.K. was finally selected. This chapter describes the characteristics of this photosensor based on [7, 16].

Table 3.1. Minimum requirements of the Hyper-K ID PMTs [7].

| Requirements	Value		Conditions
Photon detection efficiency	26%	Typ.	QE × CE at wavelength around 400 nm (including Photo-Coverage on the inner detection area)
Timing resolution	5.2nsec	FWHM, Typ.	Single Photoelectron(PE)
Charge resolution	50%	σ, Typ.	Single PE
Signal window	200nsec	Max.	Time window covering more than 95% of total integrated charge
Gain	10^7 - 10^8	Typ.	
Afterpulse rate	5%	Max.	For single PE, relative to the primary pulse
Rate tolerance	10MHz	Min.	Single PE pulse, within 10% change of gain
Magnetic field tolerance	100mG	Min.	Within 10% degradation
Life time	20years	Min.	Less than 10% dead rate
Pressure rating	0.8MPa	Min.	Static, load in water
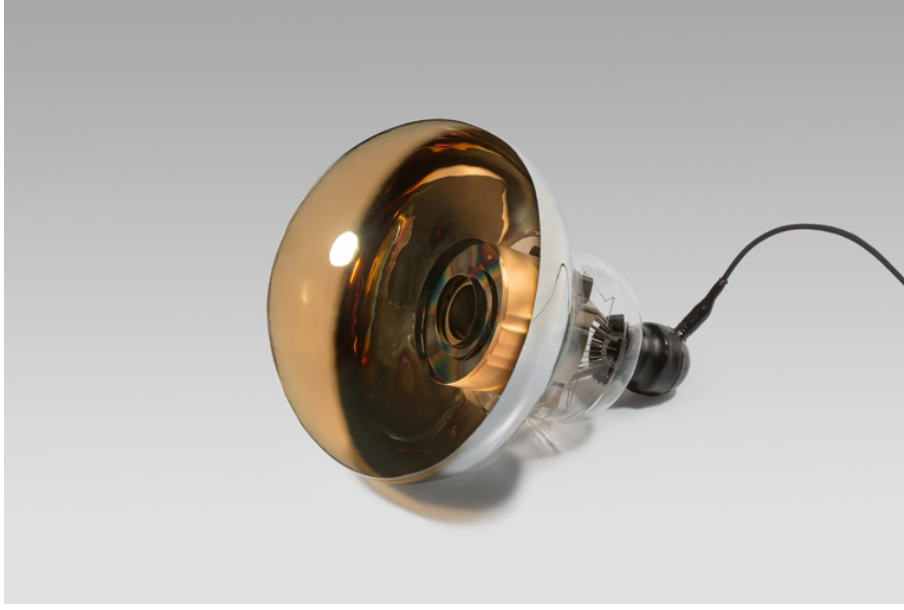
Figure 3.1. Hamamatsu R12860 PMT

3.1 R12860

The Hamamatsu Photonics (HPK) R12860 is a newly developed PMT for the Hyper-K experiment (Figure 3.1). The specifications of a typical R12860 PMT are shown in Table 3.2.

The single photoelectron time and charge resolutions of R12860 are 3.0 ± 0.2 ns and $27 \pm 4\%$, respectively, , which are a factor of two improvement from the Super-K PMT. In addition, the relative single photon detection efficiency is twice of that for the Super-K PMT. Initially, the number of dark counts increased with the improved detection efficiency. However, the number of radioactive impurities in the glass was roughly halved, and the emission of radioactive radon, which is the luminous background in the water, was significantly reduced so that the dark count rate was reduced to 4 kHz, the same level as the Super-K PMT. The materials and outline shape have been improved to withstand the depth of the Hyper-K water tank, and the water pressure resistance strength has also been doubled.

Table 3.2. Specifications of R12860 [7].

Shape	Hemispherical
Photocathode area	50 cm diameter (20 inches)
Bulb material	Borosilicate glass (about 3mm)
Photocathode material	Bialkali (Sb-K-Cs)
Quantum efficiency	30% typical at $\lambda = 390$ nm
Collection efficiency	95% at 10^7 gain
Dynodes	10 stage box-and-line type
Gain	10^7 at around 2000 V
Dark pulse rate	about 4kHz at 10^7 gain (13 °C, after stabilization for a long period)
Weight	9 kg (without cable)
Volume	61,000 cm^3
Pressure tolerance	1.25 MPa water proof

3.2   Design of R12860

Figure 3.2 shows a side view of the R12860 PMT. Its shape is similar to the PMT used in Super-K, but the curvature of the neck and photocathode has been relaxed, and the radiation in the glass has been lowered significantly. A typical bias voltage of 2,000 V is divided across each dynode by the PMT base circuit as shown in Figure 3.3. The R12860 PMT has changed its dynode structure from the venetian blind type of Super-K PMT to what is called a Box&Line type. Box&Line is the dynode arrangement shown in Figure 3.4. The largest first dynode plate is called the "Box" and has large photon coverage. A series of smaller plates are called the "Lines" and help to improve time resolution by reducing the variation of electron orbitals.
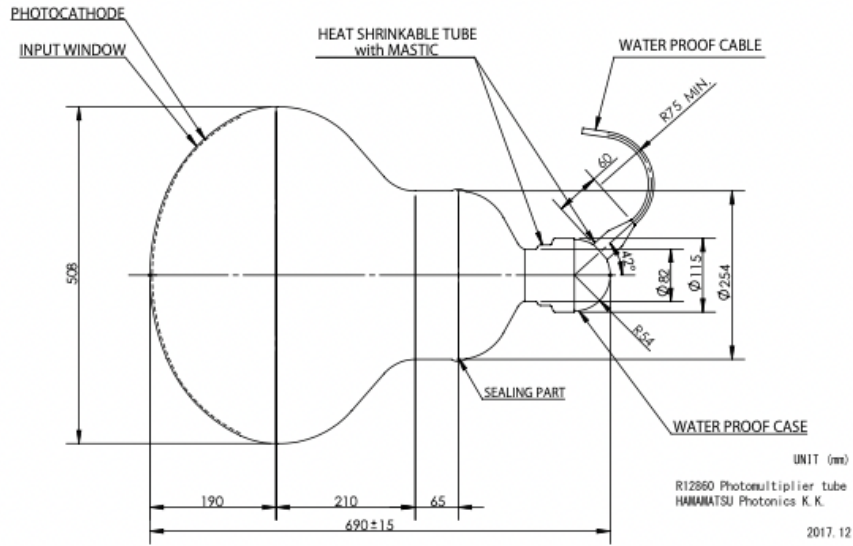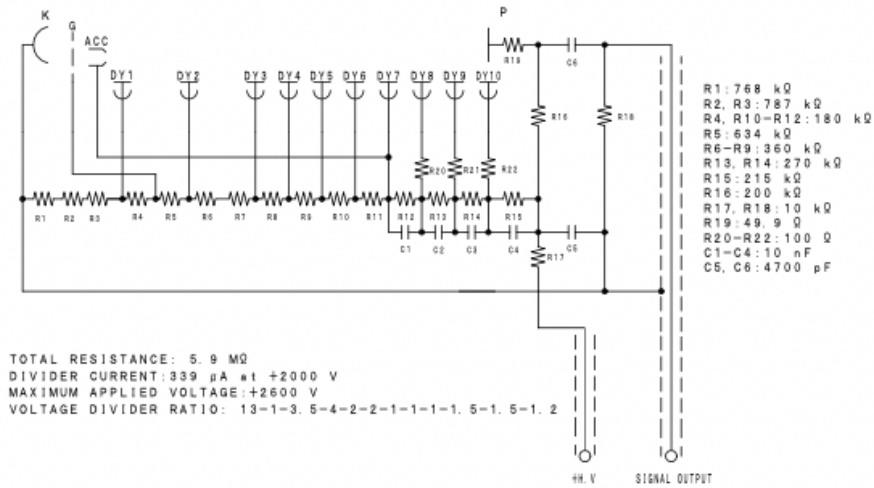
Figure 3.2. Side view of the R12860 PMT [7].

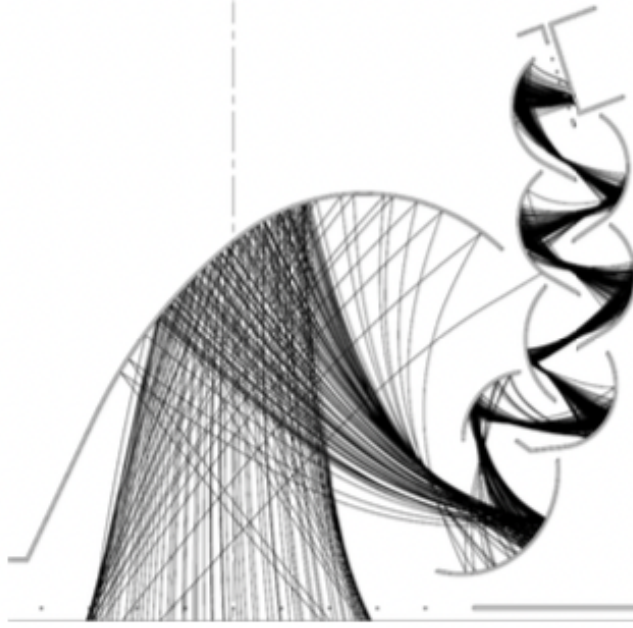Figure 3.3. PMT base circuit of R12860 PMT [7].

Figure 3.4. Box & Line dynode [17].

3.3 Photon Detection Efficiency

The photon detection efficiency of R12860 is about 32%. The detection efficiency is classified into quantum efficiency (QE) and collection efficiency (CE). The average QE of the R12860 is 33.7%, which is 1.5 times higher than that of the Super-K PMT. This is due to a change in the manufacturing process of the photocathode and the ability to manufacture the photocathode with less individual variation. Figure 3.5 shows the measured QE of R12860 as a function of wavelength, compared with the typical QE curve (dotted line) of the Super-K PMT (R3600). The shape of the QE wavelength distribution with sensitivity from 300 to 650 nm remained the same, while the peak value around 400 nm has improved from 22% to 33%.
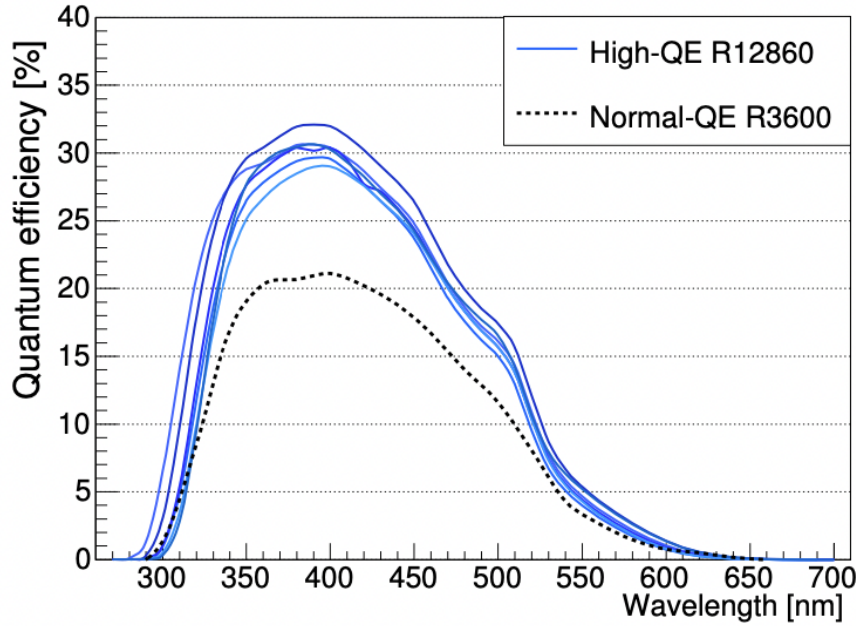
Figure 3.5. Measured QE values for six HK-PMT(R12860) and Super-K PMT(R3600).

The improvement in CE is also a major contributor. The R12860 achieved a CE as high as 95%, while the Super-K PMT had a CE of 68%. This high CE was achieved by optimizing the curvature of the glass and focusing electrodes, in addition to using the box-and-line dynodes. Compared to the Super-K PMT, the QE and CE of the R12860 are a factor of 1.5 and 1.4 higher, respectively, and the combined total detection efficiency of the R12860 is 2 times higher.

3.4   Time and Charge Resolution

Time resolution was improved by aligning electron orbitals with "Line" dynodes. The transit time spread (TTS) caused by the difference in electron traveling time is 1.23 ns for R12860, which is better than 50% of Super-K PMT's 2.86 ns (Figure 3.6). The pulse became sharper and faster, and the rise time (10% to 90%) of SPE pulses in the R12860 is about 6 ns, 40% smaller than that in the Super-K PMT.

The charge resolution of a single photoelectron is primarily due to fluctuations in the number of electrons collected at the anode. The R12860 has a higher applied voltage on the first dynode, which increases the gain of the first dynode. In addition, the collection efficiency from the first dynode to the second dynode is also improved. As a result, the charge resolution of the R12860 is improved to 35% compared to 50% of the Super-K PMT. Figure 3.7 shows the single photoelectron distribution with pedestal.
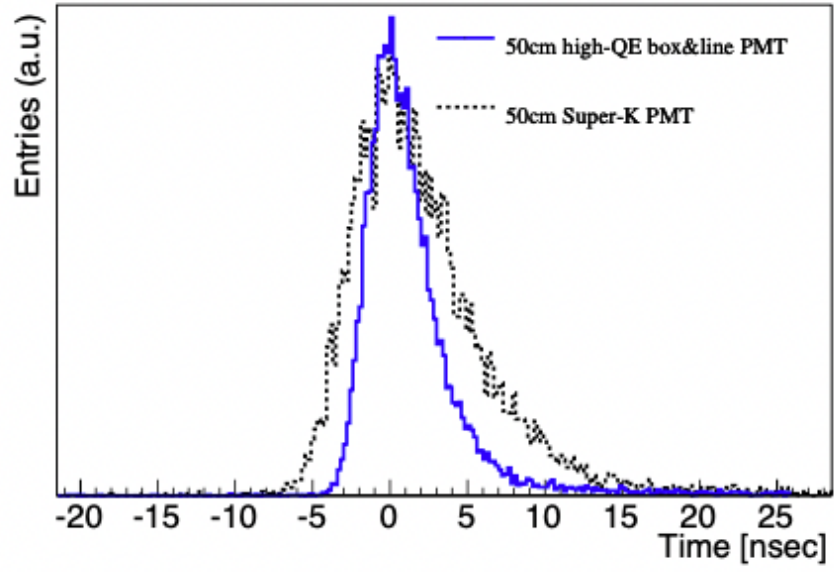
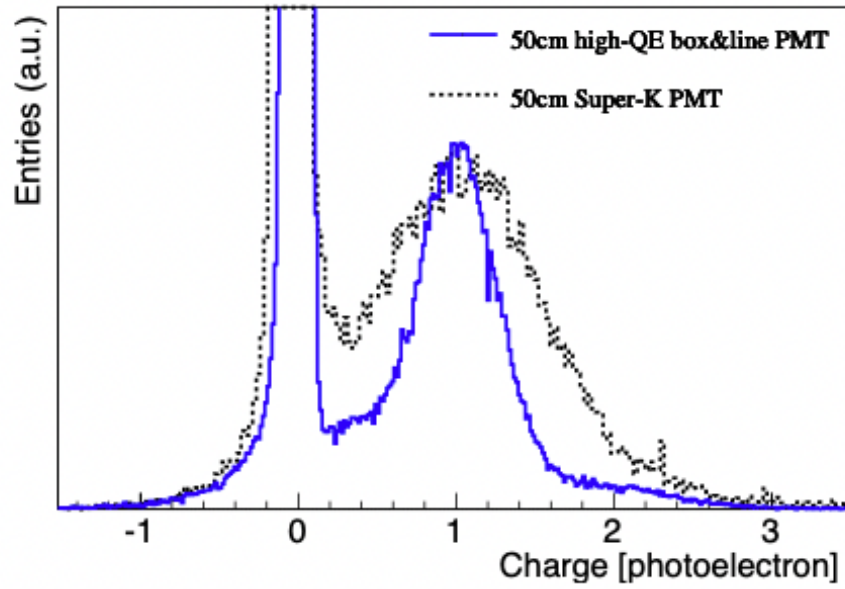Figure 3.6. Transit time distribution,compared with Super-K PMT in dotted line
[7].

Figure 3.7. Single photoelectron distribution,compared with Super-K PMT in
dotted line [7].

3.5   Afterpulse and dark hits

The main sources of background noise that can affect physical observations are afterpulses and dark hits.

The afterpulse is caused by the backflow of positive ions produced when accelerated electrons collide with residual gas in the vacuum. Different gas components have different time delays, ranging from tens of ns to tens of μs. Since the afterpulse appears at a delayed timing along with the main signal, it becomes noise when observing delayed signals such as electrons produced by the decay of muons. In the box&line PMT, the dynode is widely opened on the photocathode side, so the backflow of gas ions is more likely to occur. Therefore, attempts were made to reduce the after-pulse rate by adjusting the shape of the dynode and removing residual gas inside. Finally, the after-pulse rate of R12860 was 5% per single photoelectron.

Most PMT hits in water are dark counts. The dark count primarily arises from the thermal electron emission of the photocathode when the PMT is placed in the dark environment. Thermal electrons are emitted randomly from the entire photocathode and the amplitude of dark counts is expected to be at the single photoelectron level. In addition, dark counts can depend on the working function of the material, applied voltage, temperature, etc. Initially, a high dark rate was observed in R12860 due to the side effects of higher QE. Over a period of five years, the manufacturing process and the glass was improved, eventually successfully reducing the dark rate to below 4 kHz. This 4 kHz is the value required to achieve Hyper-K's physical goal.

Chapter 4

Detector Calibration

Detector calibrations are important to characterize the response of the Hyper-K detector. Various calibration methods have been developed and operated in the Super-K experiment. The Hyper-K, the successor of the Super-K, will take over these methods.

4.1 Inner Detector Calibration

Calibration for the detector system includes calibration on the PMT response and calibration on the optical properties of water, PMT glass, and black sheets.

 The Hyper-K detector will be calibrated based on the calibration techniques that have been done for the Super-K detector. Table 4.1 summarizes the examples of calibration items in Super-K and their calibration sources. Calibration of these items is just as important in Hyper-K calibration. In the following, we will discuss in particular the calibration of "photo-detection efficiency", "single photo-electron charge (gain)", and "light transparency of water (absorption, scattering)" in Super-K. This chapter is based on [18, 19, 20].

Table 4.1. Calibration items and calibration sources used in Super-K.

Calibration items	Calibration sources
Photo-detection efficiency	NiCf source
Gain	NiCf source
High-voltage tuning	Xe flash lamp
Timing resolution	Nitrogen-dye laser
Light transparency of water (absorption, scattering)	Nitrogen laser, laser diodes, Xe flash lamp

4.1.1 Photo-Detection Efficiency

Most low energy physics events such as solar neutrinos and diffuse supernova background neutrinos consist of 1 photoelectron (p.e.) hits. Therefore, the calibration of relative photo detection efficiency is important in the analysis of low energy
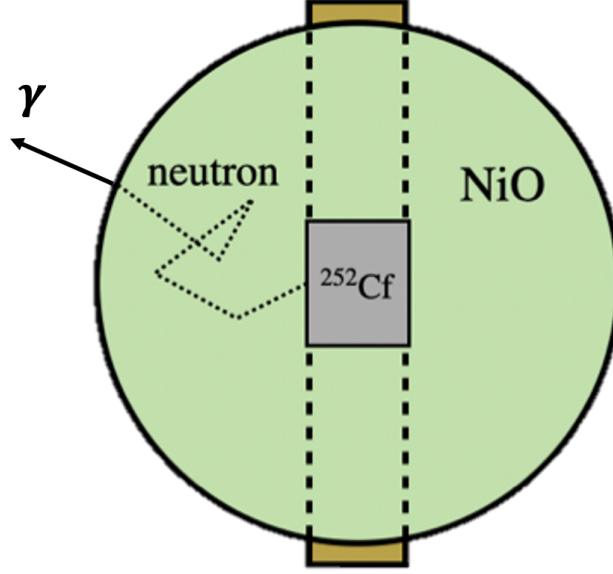
Figure 4.1. NiCf source.

physics. As shown in Table 4.1, photo detection efficiency is calibrated using a Nickel-Calfornium(NiCf) source. This nickel source is a ball made of nickel oxide and polyethylene with californium 252 (^{252}Cf) placed in the center of it, as shown in Figure 4.1.

This NiCf source uses ^{252}Cf as a neutron source. The neutrons are captured by a neutron capture reaction (^{58}Ni(n, γ)^{59}Ni), and gamma rays of about 9 MeV are isotropically emitted. This gamma ray induces electron-positron pair production and Compton scattering, resulting in the emission of a single photoelectron level of Cherenkov light in water. Since this Cherenkov light is emitted isotropically, the relative photo detection efficiency (quantum efficiency × collection efficiency) of each PMT can be calibrated by comparing the difference in hit rates between PMTs.

4.1.2 Single Photo-electron Charge (Gain)

Gain calibration is performed in two steps. First, the relative differences between PMTs are measured. This relative gain correction is then applied to obtain the average gain of the entire detector. Once the average gain and the deviation of each PMT from that average are known, the gain of each individual PMT can be obtained.

A nitrogen-laser-driven dye laser is used as the light source to measure the relative gain. The measurement is done in two steps. First, a high-intensity flashes are used to ensure that all PMTs receive a sufficient number of photons. The average value of the charge of the PMT i is denoted as $Q_{obs}(i)$. In the subsequent

measurement, a low-intensity flashes are used so that the PMTs receive only a very small number of photons. Let $N_{obs}(i)$ be the number of times the PMT i records a charge above the threshold. These two measurements are performed with the same light source and at the same position in the tank.

$$Q_{obs}(i) \propto I_s \times a(i) \times \epsilon_{qe}(i) \times G(i), \tag{4.1}$$

$$N_{obs}(i) \propto I_w \times a(i) \times \epsilon_{qe}(i). \tag{4.2}$$

Here, I_s and I_w are the average intensity of high-intensity and low-intensity flashes, respectively, $a(i)$ is the acceptance of PMT i, $\epsilon_{qe}(i)$ is its QE, and $G(i)$ is its gain. The gain of each PMT can be calculated from the ratio of equations 4.1 and 4.2.

$$G(i) \propto \frac{Q_{obs}(i)}{N_{obs}(i)}. \tag{4.3}$$

The relative gain of each PMT can then be obtained by normalizing by the average gain of over all PMTs. By using the continuous distribution of relative gain corrections obtained here, the cumulative single-photoelectron distribution for all PMTs can be created. This distribution approximately represents the average single-photoelectron response of the detector. From this, it is then possible to extract the absolute gain of all PMTs. The NiCf source, described in the previous section, is used to create this cumulative single-photoelectron distribution. This source is located in the center of the tank, and more than 99% of the observed signals are at the single-photoelectron level.

4.1.3 Light Transparency of Water

In the simulation of the transport of photons by MC, effects such as scattering and absorption by water in the tank must be taken into account. In this section, we discuss the measurement of water transmittance. It should be noted that the following is the model used in the Super-K experiment, and it is not certain whether it can be applied in the Hyper-K experiment in the same way.

The light in the water with a wavelength(λ) attenuates according to:

$$I(\lambda) = I_0(\lambda)\exp\left(-\frac{l}{L(\lambda)}\right), \tag{4.4}$$

where l is the length of light travel, $I_0(\lambda)$ is the initial intensity, and $L(\lambda)$ is the total attenuation length due to scattering and absorption, which is called the water transparency. $L(\lambda)$ is defined in MC as follows:

$$L(\lambda) = \frac{1}{\alpha_{abs}(\lambda) + \alpha_{sym}(\lambda) + \alpha_{asym}(\lambda)}, \tag{4.5}$$

where $\alpha_{abs}(\lambda)$, $\alpha_{sym}(\lambda)$, and $\alpha_{asym}(\lambda)$ are the attenuation coefficients for absorption, symmetric scattering, and asymmetric scattering, respectively. $\alpha_{sym}(\lambda)$ is used to introduce symmetric components of Rayleigh and Mie scattering, and

$\alpha_{asym}(\lambda)$ to introduce forward Mie scattering. $\alpha_{abs}(\lambda)$, $\alpha_{sym}(\lambda)$, and $\alpha_{asym}(\lambda)$ are expressed by the following equations based on experiments:

$$\alpha_{abs}(\lambda) = P_0 \times \frac{P_1}{\lambda^4} + C, \tag{4.6}$$

$$C = P_0 \times P_2 \times \left(\frac{\lambda}{500}\right)^{P_3}, \tag{4.7}$$

$$\alpha_{sym}(\lambda) = \frac{P_4}{\lambda^4} \times \left(1.0 + \frac{P_5}{\lambda^2}\right), \tag{4.8}$$

$$\alpha_{asym}(\lambda) = P_6 \times \left\{1.0 + \frac{P_7}{\lambda^4} \times (\lambda - P_8)^2\right\}. \tag{4.9}$$

To determine the respective attenuation coefficients, laser light of five different wavelengths (337, 375, 405, 445, and 473 nm) is injected into the tank and hit time to the PMT is measured. The attenuation coefficients are determined by comparing the hit time distribution of the MC created by varying these 9 parameters (P0 to P8) with the hit time distribution of the measured data, so that χ^2 is minimized. Figure 4.2 shows the typical fitted water coefficient functions used in the SK-MC.
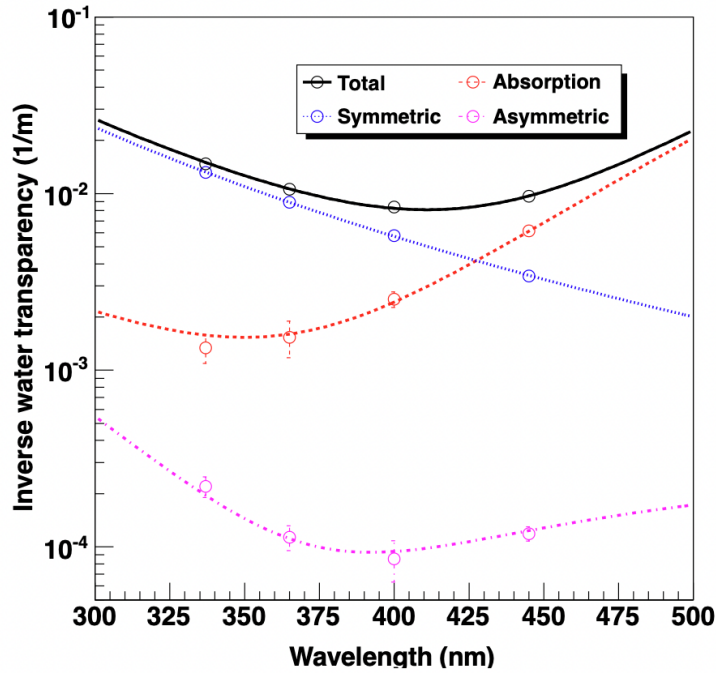
Figure 4.2. Typical fitted water coefficient function used in SK-MC. This data was obtained in April 2009. Each line through the absorption, symmetric scattering, and asymmetric scattering points represents a fitted function, and the top line shows the total of all fitted functions added together [18].

4.2 Pre-Calibration

The previous section shows calibration of PMT properties and the water in the tank in the Super-K experiment. Although many of the PMT properties and water quality can be measured and calibrated by employing multiple calibration sources inside the tank (*in-situ*), there are several items cannot be adequately measured. In this section, we describe measurements, called pre-calibrations, performed outside the tank (*ex-situ*) to investigate the more detailed performance of PMTs to complement *in-situ* measurements.

4.2.1 Motivation of the pre-calibration

Multiple parameters such as light detection efficiency vs. water transmittance, timing offset vs. PMT position can be often degenerate due to limitations of the location and type of light sources in *in-situ* calibration. Therefore, we will conduct a detailed *ex-situ* measurements for about 2% of all PMTs in advance. These calibrated PMTs will be then placed in a pre-determined locations in the tank as reference PMTs (Figure 4.3), and the degeneracy will be solved based on the performance of these reference PMTs.

As an example, in the Super-K calibration, these reference PMTs were used when determining the high voltage to be applied to each ID PMTs and ensuring that all ID PMTs output the same amount of charge. Figure 4.3 shows the location of the reference PMTs and the grouping of PMTs in the vicinity of the reference PMTs. The applied high voltage of a PMT other than reference PMTs was set so that the amount of charge obtained by that PMT matches the average amount of charge obtained by the reference PMTs belonging to that group.
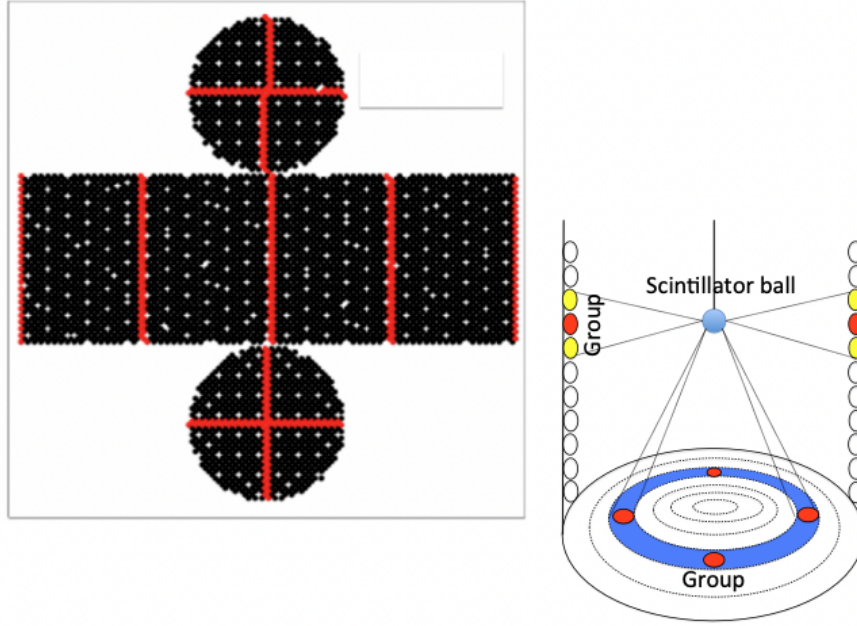
Figure 4.3. The location of the reference PMTs (left) and the schematic diagram of PMT grouping (right) in the Super-K water tank, the red points indicate the location of the reference PMTs [18].

4.2.2 Measurement Items of the pre-calibration

The items to be measured in the pre-calibration must focus on PMT performance, which has dependencies that are difficult to control in the tank (Table 4.2). For example, the dependence of quantum efficiency (QE) and collection efficiency (CE) and gain on the position of light incidence, and the dependence of QE on the light incidence angle and on the wavelength of light. The environmental difference between *in-situ* and *ex-situ* should also be carefully investigated. Temperature, magnetic field, time required for stabilization, and availability of water can vary between *in-situ* and *ex-situ*.

Table 4.2. Candidates for pre-calibration parameters.

Response Parameter	Dependent Variables difficult to control *in-situ*
QE	light incidence position and angle, light wavelength
CE	light incidence position
Gain	light incidence position

Since pre-calibration is performed in air and the actual 50-cm PMT operation is in water, it is important to evaluate PMT performance in both air and water. In addition, it is necessary to evaluate the temperature dependence of the PMT performances in advance because most of the pre-calibration will be done at room

temperature, whereas the water temperature in the tank is planned to be around 13 °C.

Therefore, in this study, we constructed a setup that allows for underwater measurements and temperature control using a water tub, a circulator, and a chiller.

This study was designed to evaluate the effect of the presence of water on PMT performance and to investigate the temperature dependence of dark rate, gain, and relative QE by varying the water temperature. The details are given in the next chapter.

Chapter 5

Performance evaluation of 50-cm PMT in an underwater environment

5.1 Overview

As mentioned in the previous chapters, the Hyper-K detector will have approximately 20,000 50-cm PMTs in the inner detector. For the Hyper-K detector calibration, it is necessary to understand the PMTs' response and establish methods to evaluate their performance before installing them (pre-calibration). Pre-calibration of 50-cm PMTs will be performed at room temperature (around 25 °C). On the other hand, the 50cm PMT will be operated at approximately 13 °C during actual operation in the Hyper-K detector. Therefore, for the calibration of the Hyper-K detector, it is necessary to predict the performance at the actual operating temperature from the measurement at room temperature, and we are currently trying to achieve this with an accuracy of better than 1%. In addition, the possible performance difference with and without water must also be evaluated in advance.

In this study, we first constructed a setup that allows underwater measurements and temperature control. Using this setup, we measured the gain, relative QE, and dark rate of the 50-cm PMT at multiple temperature points and evaluated their temperature dependence. The temperature dependence of these properties has not been measured in water before, and this study is the first result. In this chapter, we discuss these measurements and results.

5.2 Setup

This section describes the measurement setup. The equipment for the measurement includes a water tub to house the 50-cm PMT, a water purification system, a chiller, an optical system to illuminate the PMT, and various measurement instruments to acquire data such as PMT signal and temperature. Figure 5.1 is a schematic diagram of the setup for this measurement. Table 5.1 summarizes the items used in the measurements.
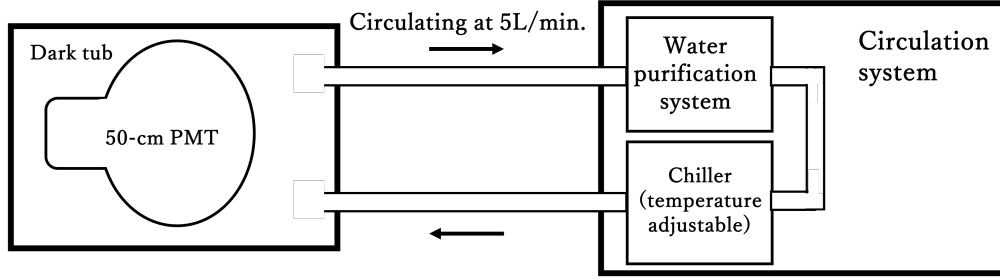
Figure 5.1. Schematic diagram of the setup. The water tub is connected to a circulation system by hoses.

Table 5.1. List of instruments used in the measurement

Use	Manufacturer	Model Number
HV(for HK PMT)	HAYASHI-REPIC	RPH-011
HV(for monitor PMT)	Stanford Research Systems	PS350/5000V
ADC	CAEN	DT5761
NIM crate	HAYASHI-REPIC	RPN-005-153
AMP	HAYASHI-REPIC	RPN-093
Function generator	Agilent	33250A
1 inch PMT	HAMAMATSU	R7378A
Laser diode head	HAMAMATSU	M10306-29
Oscilloscope	TELEDYNE LECROY	Wavesurfer 3034z
thermometer	T and D	TR-72nw
	T and D	TR-71nw
thermometer Probe	T and D	TR 1220
Half mirror	Edmund	polkadot 50R/50T 46459
Gauss meter	Lutron	GU-3001

5.2.1 Dark Tub

Our measurements were conducted using a specially designed stainless steel water tub (hereinafter referred to as "dark tub"). The tub is equipped with posts and rubber bands to securely hold the PMT, and a pedestal for placing light sources (Figure 5.2a). The tub has a capacity of up to 525 liters. Magnetic shield panels are attached to each side of the tub. The specifications for this tub are listed in Table 5.2.

The inside of the tub is covered with black sheets to suppress light reflection(5.2b).

Table 5.2. Specifications of dark tub

Size	
external dimensions	1102× 852× H982 [mm]
internal dimensions	1004× 754× H822 [mm]
Mass	
tub	230 [kg]
with full of water	730 [kg]
Material	
inside tub	SUS304
outside and lid	SUS304 and anodized aluminum
shield	soft magnetic alloys (Permalloy PC)
Capacity	525 [L]
Magnetic Shielding Effect	
geomagnetism	1/5 - 1/10
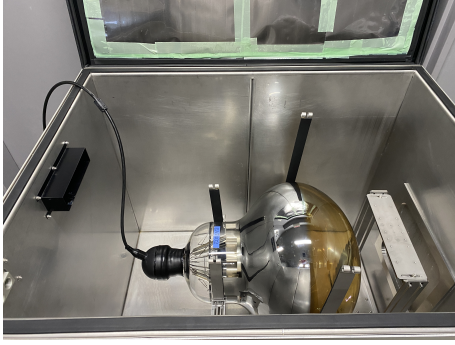
(a) PMT mounted on the dark tub.   (b) Black sheets and thermometers.
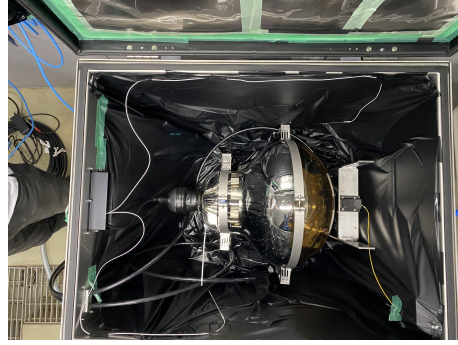
Figure 5.2. Inside the dark tub

PMTs with a large-aperture photocathode, such as the 50-cm PMT, are easily affected by magnetic fields, which bend the trajectory of the photons. Therefore, it is necessary to consider the effect of even geomagnetic-level magnetic fields on the photoelectron collection. We measured the residual geomagnetic field near the PMT photocathode and the results are shown in Table 5.3. It was confirmed that the total magnetic field is suppressed to less than 100 mG. Directions of x, y, z are defined as shown in Figure 5.3. This value is within the performance guarantee range of this 50-cm PMT.

5.2.2   Water circulation system

To reproduce the actual conditions in the Hyper-K tank, the water in the tub must be pure. In this measurement, we adopted a water purification system and used it to recirculate the water in the tub. Figure 5.4 is a picture of the purification system, and Figure 5.5 is a schematic diagram of the whole water circulation system, including the purification system. This water purification system consists of
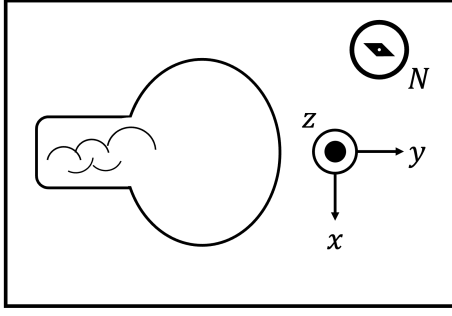
Figure 5.3. View of 50-cm PMT and the dark tub from the top.

Table 5.3. Measured residual geomagnetic field, the directions are shown in Figure 5.3.

Direction	Value [mG]
x	-48
y	-58
z	-22
total	78

multiple filters, ion exchange resins, and organic matter decomposers. The system is equipped with sensors at several locations, and the water temperature and conductivity at each location are monitored. In addition, this system incorporates a chiller, which control the water temperature while circulating the water. The water temperature can be set freely between 12 °C and 30 °C. The dark tub is connected to this water purification system by hoses. To avoid being affected by outside temperatures, the dark tub and hoses are each covered with insulation material.

First, about 500 liters of tap water was filled into the tab. The water was then circulated and purified at a flow rate of 5 liters per minute using the purification system. Since we aim to measure the temperature dependence of various PMT performances by varying the water temperature, the water temperature must be properly controlled. As mentioned above, the water temperature is controlled by a chiller built into the circulation system.

Then, we tested how the water temperature in the tub changes when the chiller temperature is changed, and whether the water temperature is stable while the chiller temperature is fixed. A water-resistant thermometer Ondotori TR-1220 was used to measure temperature in water. We placed this thermometer in two locations: one (Ch.1) at the height of the bottom of the photocathode and the other (Ch.2) at the height of the top of the photocathode as shown in Figure 5.6. Figure 5.7 shows the water temperature transition. The point of rapid temperature change was at the point where the chiller setting was changed. It was found that while the chiller temperature was fixed, the temperature at each height was stable within ±0.1 °C and the maximum temperature difference between the top and bottom of the photocathode was 0.2 °C. Similarly, while the water temperature was changing, temperature difference of up to 0.2 °C between the top and bottom.

Figure 5.4. Water purification system.
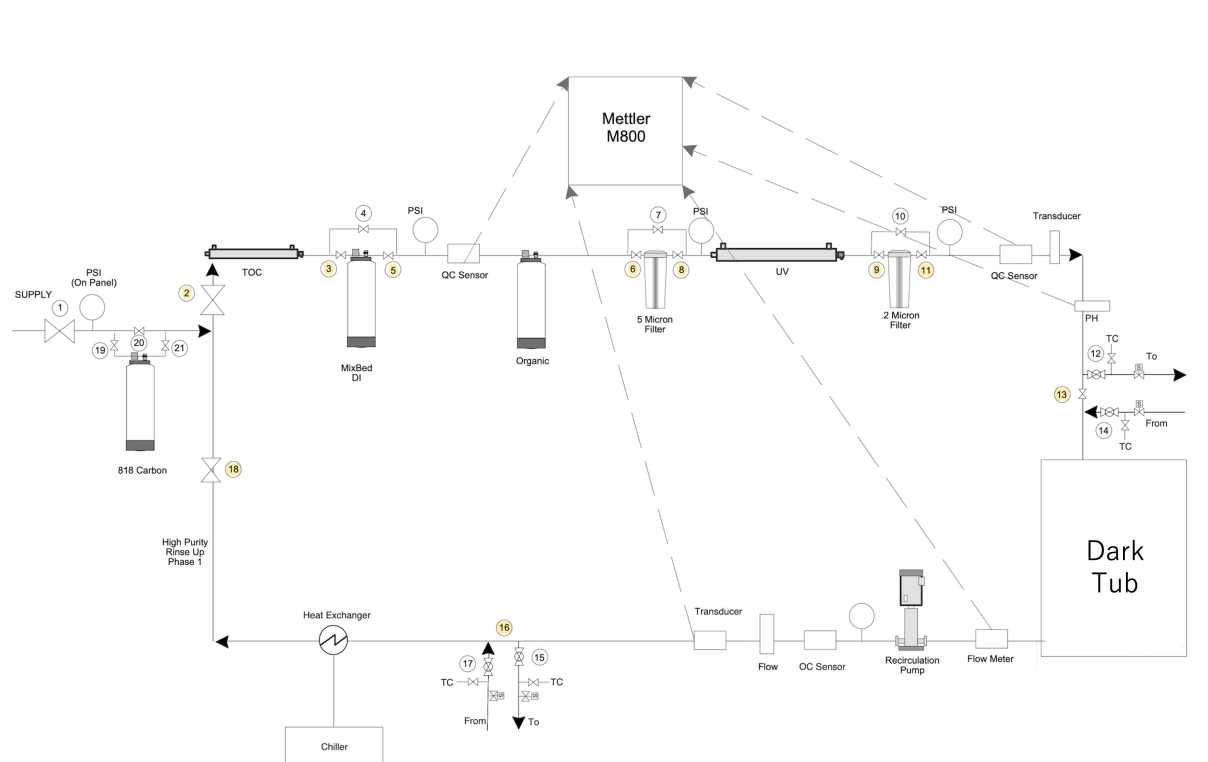
Figure 5.5. Schematic diagram of the water circulation system.
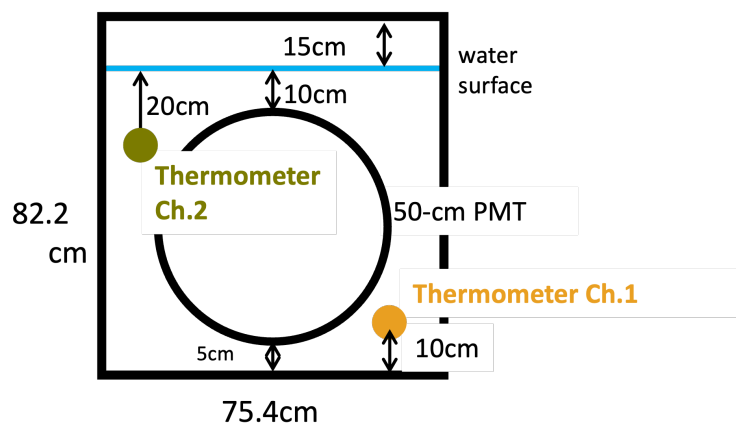
Figure 5.6. Arrangement of thermometers when looking at the photocathode from the front.
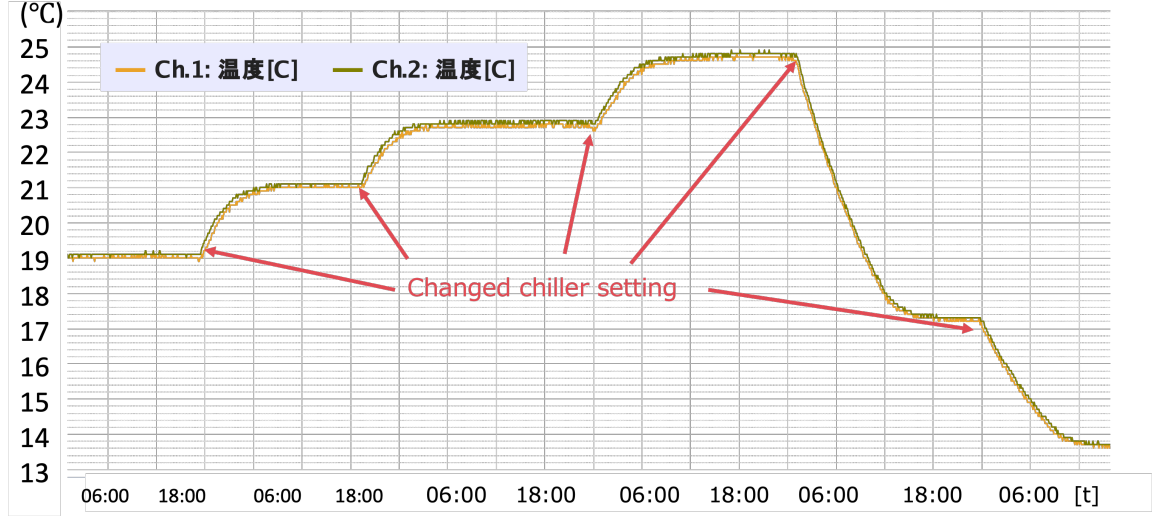
Figure 5.7. Water temperature transition.

5.2.3 Light injection system

Laser light with a wavelength of 410 nm and a pulse width of less than 50 ps was used as the light source. In this measurement, the laser beam is divided into two; one is to be injected to the 50-cm PMT, and the other is for monitoring the light yield. To transport the laser light, an FC-FC fiber was used.

Figure 5.8 shows the schematic of light injection system. First, the light emitted from the laser source is guided through the fiber and onto the optical table. On the optical table, the laser beam first passes through a collimator lens to prevent it from diffusing, and then the laser beam is split in two by passing through a beam splitter. One of the beams is then irradiated onto the 1-inch PMT, and the other is focused by another collimator lens and again injected to a fiber. This entire optical system is installed in a dark box (Figure 5.9).
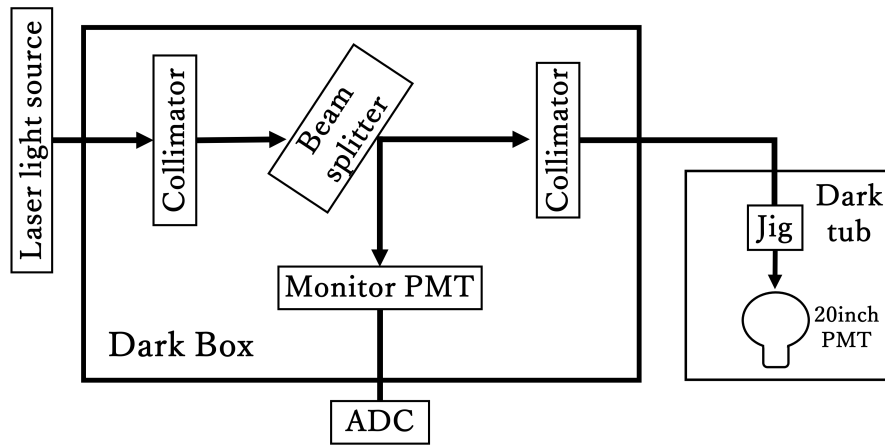
Figure 5.8. Schematic of light injection system.

40
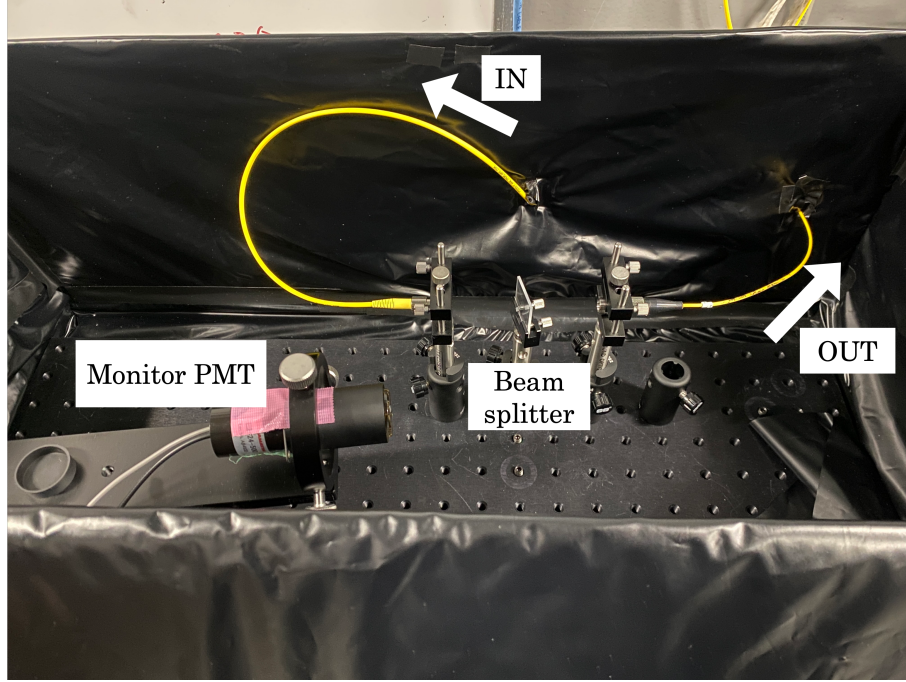
Figure 5.9. Optical table, optical equipment, and optical components in a dark box.

The fiber exiting the dark box is introduced into the dark tub through a window on the side of the tub. The fiber ends are attached to specially designed jigs (Figure 5.10). This jig was created with a 3D-printer, and can secure the fiber to the pedestal inside the tub. Figure 5.11 shows the inside of the tub.
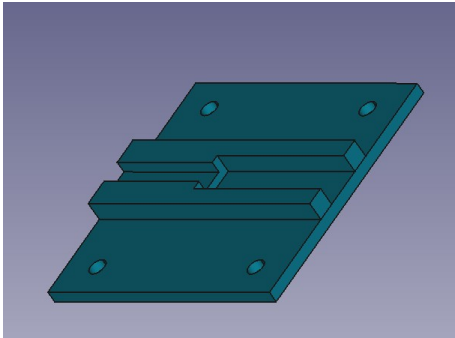
Figure 5.10. 3D data of jig.

Figure 5.11. Fiber fixed to pedestal.

5.2.4   DAQ system

A schematic diagram of the entire DAQ is shown in Figure 5.12. Throughout this measurement, a voltage of 1840 V is applied to the 50-cm PMT so that its gain is approximately 1×10^7. Signals from 50-cm PMT were acquired using a flash ADC, CAEN DT5761 (Figure 5.13) [21]. This flash ADC is a desktop module housing 1 Channel 10 bit 4 GS/s digitizer with 1 Vpp dynamic range. The

ADC was controlled by WaveDump [22]. WaveDump is a console application for data acquisition of CAEN digitizers with waveform recording firmware. Waveform information can be recorded with a set of configurable parameters defined by a external text file. For 50-cm PMT signal acquisition, a ×10 signal amplifier was used just before the digitizer. This was done to improve the charge resolution.
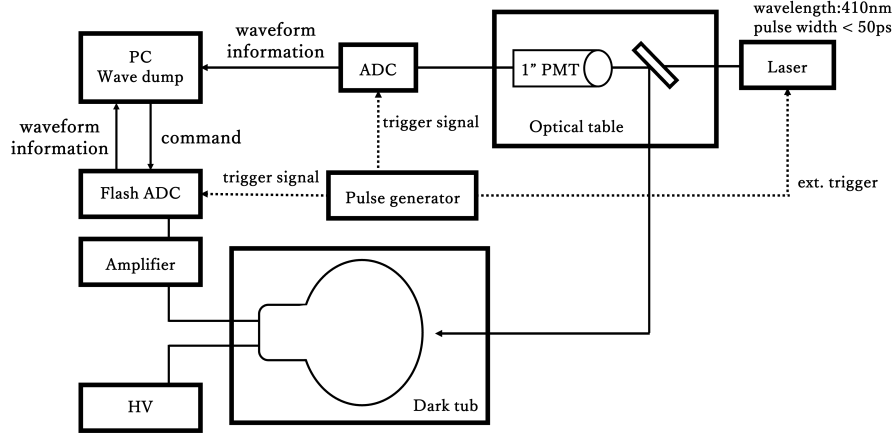
Figure 5.12. DAQ schematic

Figure 5.13. CAEN DT5761.

Figure 5.14. Wavesurfer 3034z.

To read out signals from monitor 1-inch PMT, we employed Teledyne's wavesurfer 3034z as the ADC (Figure 5.14). This is an oscilloscope capable of recording waveforms, with a sampling rate of up to 4GS/s, and the vertical resolution of 8bits with 17 mVpp dynamic range.

A pulse generator was used as an external trigger for the emission of the laser. Signals synchronized with the emission timing of this laser were then used as the trigger for the two waveform digitizers. The frequency of the pulse generator was 4000 Hz.

Figures 5.15a and 5.15b show examples of 50-cm PMT and 1-inch PMT waveforms, respectively. For 50-cm PMT, waveform information was recorded for 1000 ns per trigger event, and WaveDump was set so that the PMT signal originating from the laser light would be around 850 ns of the time window.
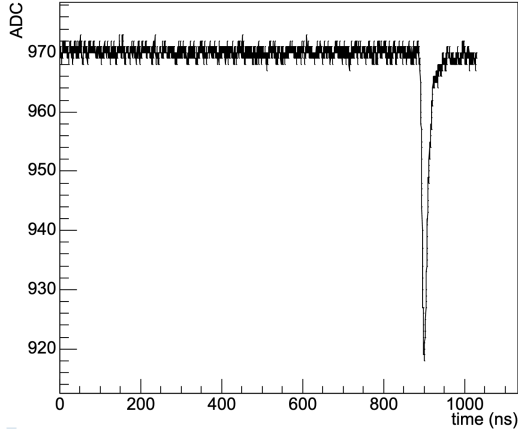
(a) Waveform of 50-cm PMT.　　　(b) Waveform of 1-inch PMT.
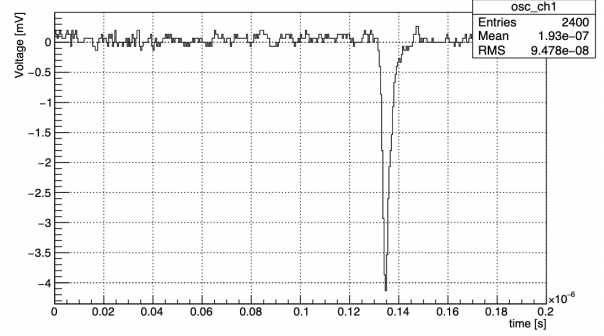
Figure 5.15. Examples of Waveform

5.3　Data taking

This section describes the data common to all gain, relative QE, dark rate measurements. These data were acquired from December 21 to 30, 2023.

5.3.1　50-cm PMT operation and data taking

Figure 5.16 plots the water temperature and applied high voltage to 50-cm PMT for the measurement period, and each point is the average of the data for every 15 minutes.
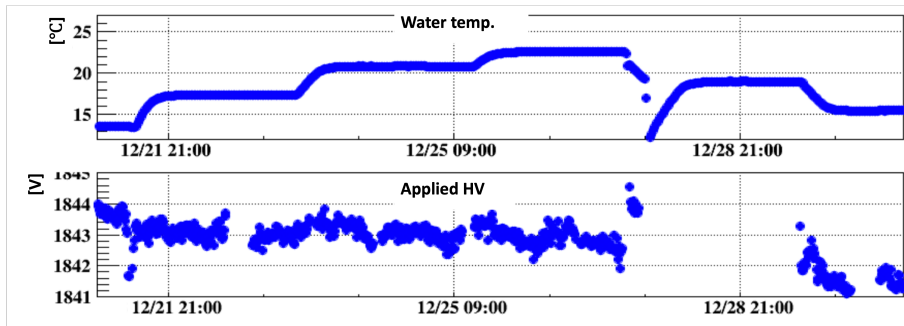
Figure 5.16. Water temperature (upper) and applied high voltage to 50-cm PMT (lower) during the data taking.

The chiller setting was changed in the order of 13 ℃, 17 ℃, 21 ℃, 23 ℃, 19 ℃, and 15 ℃. After the 23 ℃ underwater measurement, the water was once drained from the tub and the gain measurement was taken in the air, then the

water was filled again and the underwater measurements were taken. All underwater measurements were taken at least 12 hours after the water temperature had stabilized. Measurement duration at each temperature is summarized in Table 5.4. The temperatures in Table 5.4 are the values of the thermometer in the tub (except for the measurement in air).

Table 5.4. Measurement duration at each temperature

temp. [°C]	13.5	15.1	17.5	19.3	21.1	22.9 (in water)	23 (in air)
time [hour]	5.5	4.5	2.5	2.0	5.0	3.0	1.75

The applied voltage is one of the factors that affect gain. As shown in Figure 5.16, we observed a fluctuation of the applied voltage of ± 2 V. In general, the gain μ is proportional to the kn power of the applied voltage V. Here, k is determined by the structure and material of the dynode and takes the value of 0.7 - 0.8, and n is the number of dynodes.

$$\mu \propto V^{kn} \tag{5.1}$$

Hereinafter, with $k = 0.8$ and $n = 10$, measured 50-cm PMT gain is corrected to that of 1843.5V using Equation 5.1.

In addition to the correction of applied voltage, for more accurate measurements, the influence of the surrounding environment on the measurement must also be considered. First, we investigated the relationship between the ambient temperature of the digitizer and gain variation. Figure 5.17 plots the variation of gain versus the ambient temperature around the digitizer at a certain water temperature along a time series. It was observed that as the digitizer's ambient temperature decreased, the gain decreased accordingly, and as the former increased, the latter increased as well. We therefore took a countermeasure using the calibration function of digitizer.

This CAEN's digitizer is automatically calibrated for temperature changes at startup. However, since this calibration is performed only at startup, if a temperature change occurs during the measurement, the measurement may be performed without being properly calibrated. Then, we changed the data taking procedure to restart the digitizer every 30 minutes during the measurement to minimize the effect of temperature change.
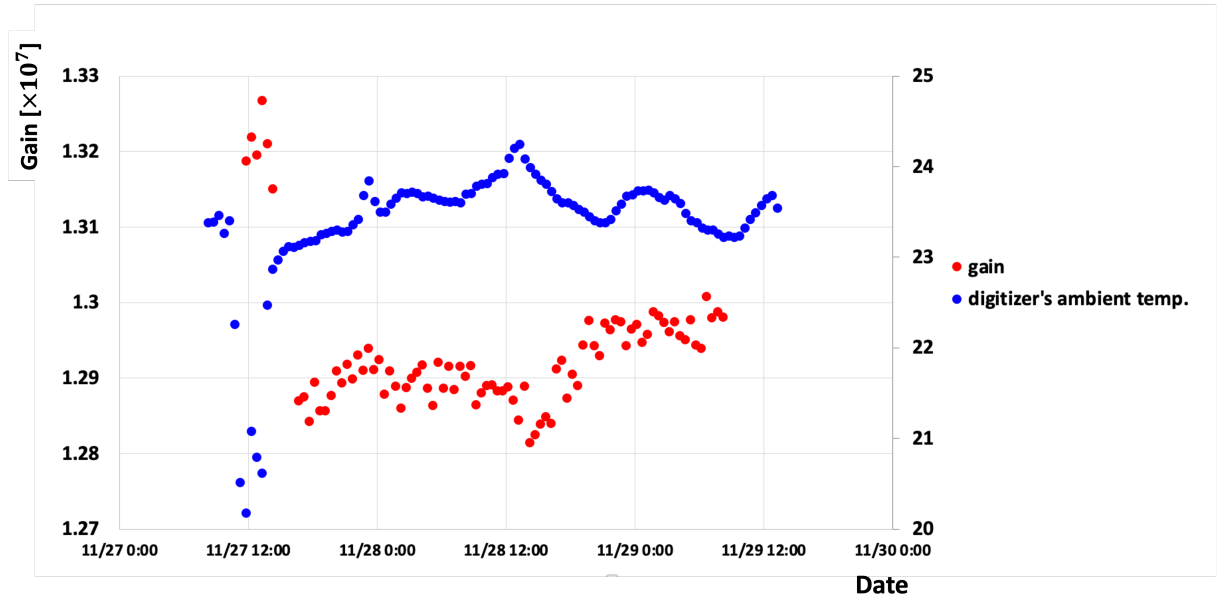
Figure 5.17. Gain change and temperature change of the digitizer.

5.3.2 Laser light intensity monitoring

The light yield of the monitor PMT is defined and derived as follows;

1. Figure 5.18 shows an example of monitor PMT signal. For every single waveform data, the ADC values between 0 - 120 ns are added together and averaged, which is defined as the baseline. Then, for the ADC values of the 125 - 150 ns waveform, Σ(ADC value - baseline) is calculated to obtain the integral value of the charge.
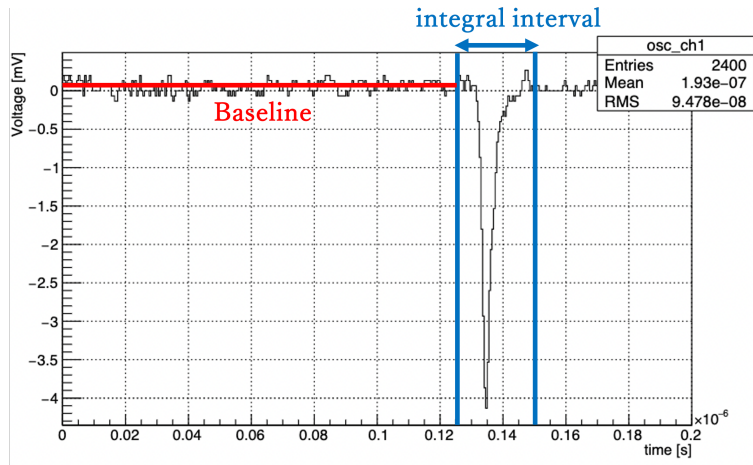
Figure 5.18. Monitor PMT Signal with baseline and integral interval.

2. The distribution of the charges obtained in 1. is shown in Figure 5.19. The signals with integral values greater than 100 mV were eliminated to remove events with direct cosmic ray incidence on the PMT. The amount of events at around 0 is consistent with the expectation assuming the Poisson distribution with the average of 3 photoelectrons. The average value of this distribution is defined as the light yield of the monitor PMT and hereafter referred to as the "monitor light yield".
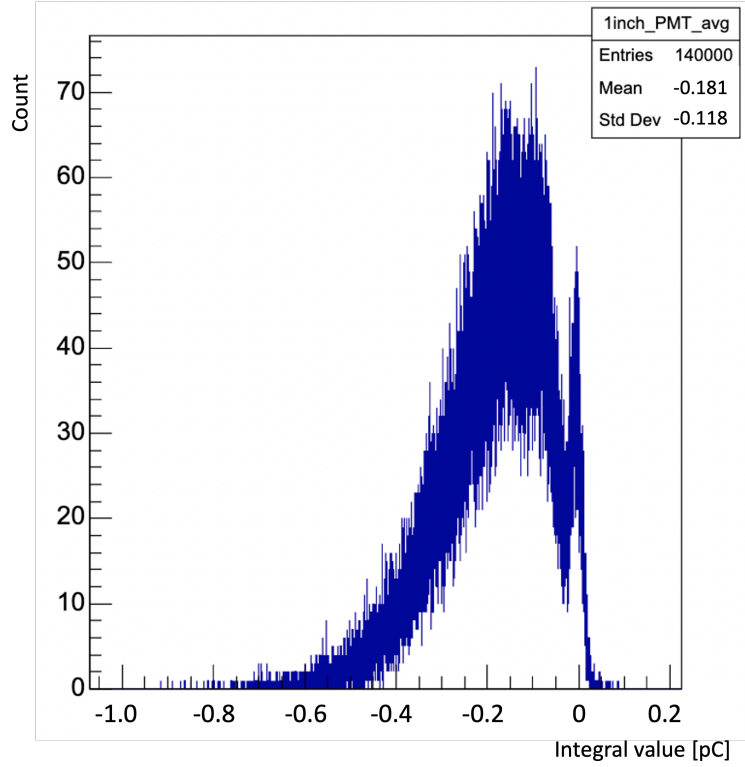
Figure 5.19. Charge distribution of monitor PMT.

In monitor light yield measurement, the laser's ambient temperature was monitored by a thermometer, Ondotori TR-72nw. Figure 5.20 plots the laser's ambient temperature data and monitor light yield for the measurement period, and each point is the average of the data for every 15 minutes.
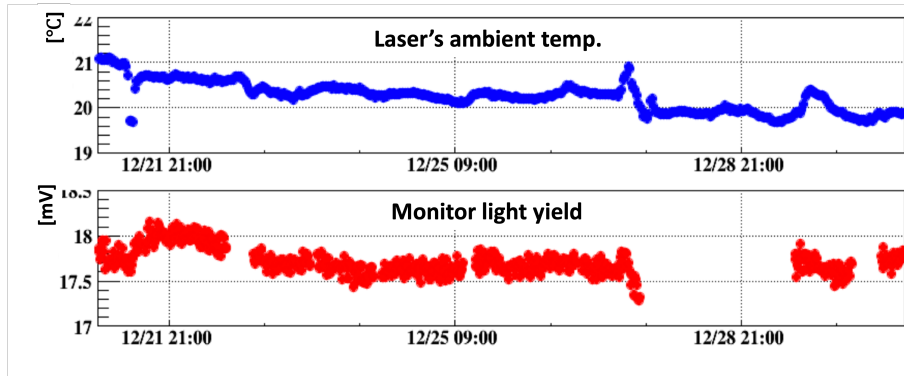
Figure 5.20. The upper is the laser's ambient temperature and the lower is the monitor light yield.

Figure 5.21 plots the average laser's ambient temperature on the horizontal axis and the average monitor light yield on the vertical axis during each water temperature measurement period. This result shows that the monitor light yield was stable in the range of $\pm 1\%$ during the measurement period. Since the monitor light yield was stable at $\pm 1\%$, we concluded that the laser light intensity itself was also stable within $\pm 1\%$.
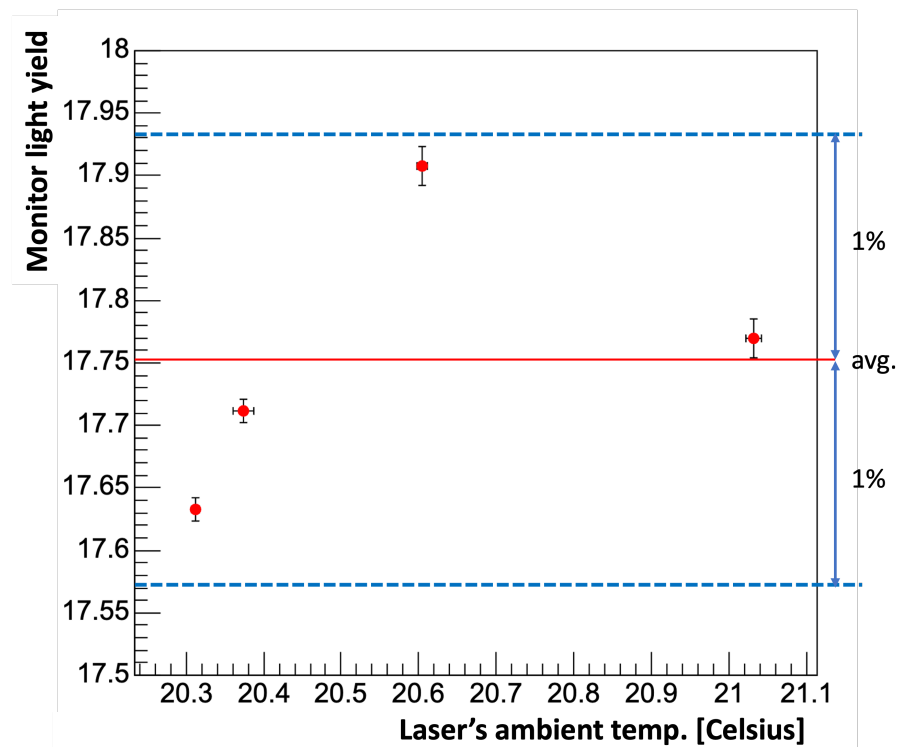
Figure 5.21. Comparison of monitor light yield at different laser's ambient temperatures.

5.4   Results

5.4.1   Temperature dependence of gain

To determine the gain, the integral value of the charge is calculated from the obtained waveform. Figure 5.22 shows an example of laser-derived signal waveform. The current setup is adjusted so that the laser-derived signal is in the 850 - 950 ns range. For every single waveform data, the ADC values between 750 - 850 ns are added together and averaged, which is defined as the "baseline". Then, for the ADC values of the 850 - 950 ns waveform,

$$\Sigma(\text{baseline -ADC value}) \text{ [mV]} \times 0.25 \text{ [ns]} / 50 \text{ [}\Omega\text{]} / 10$$

is calculated to obtain the integral value of the charge. Here, 0.25 ns comes from the digitizer's sampling rate (4 GS/S), and 50 Ω comes from the digitizer's input impedance, and 10 is the amplification factor of the amplifier.
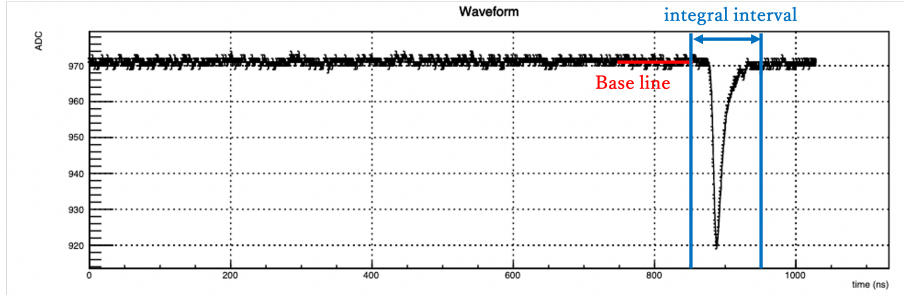
Figure 5.22. Laser-derived signal waveform

A single photoelectron charge distribution (SPE distribution) is then created from the calculated charge. The obtained histogram was fitted with the following equation:

$$f_{(x)} = \left\{ p_0 e^{-\left(\frac{x-p_1}{p_2}\right)^2} + p_{10} e^{-\left(\frac{x-p_1}{p_{11}}\right)^2} \right\} + p_3 e^{-\left(\frac{x-p_4}{p_5}\right)^2} + p_6 e^{-\left(\frac{x-p_7}{p_8}\right)^2}$$
$$+ p_9 \left\{ \text{erfc}\left(\frac{x-p_4}{p_5}\right) - \text{erfc}\left(\frac{x-p_1}{p_2}\right) \right\}$$
$$(5.2)$$

where p_i for $i = \{0, 11\}$ is the fitting parameter and erfc stands for the Gaussian complementary error function. The first two terms fit the pedestal, and the third and fourth terms perform single-photon and two-photon peak fitting, respectively. The error function terms were used to fit the "valley" between the pedestal and the one-photon peak. An example of this fitting results is shown in Figure 5.23.
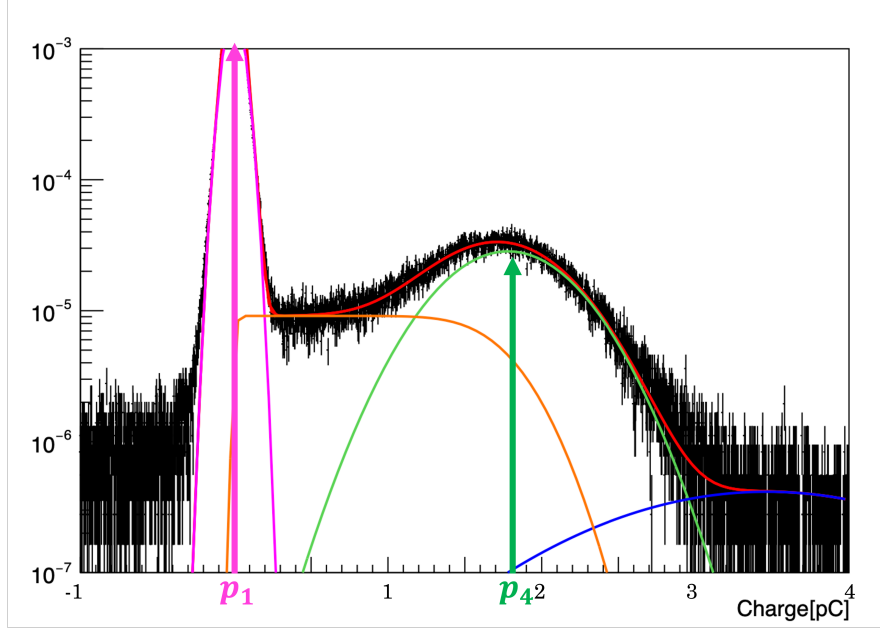
Figure 5.23. An example of fitting of SPE distribution Magenta represents the pedestal fit, and green and blue represent the fit of the single-photon and two-photon peaks, respectively. Histograms of charges are normalized.

The gain is defined as the average charge corresponding to a single photoelectron (in this case $p_4 - p_1$) divided by the elementary charge e (1.6×10^{-19} C).

$$\text{gain} = \frac{p_4 - p_1}{1.6 \times 10^{-19}} \tag{5.3}$$

We measured at six temperature points in a range from 13 °C (close to the HK water temperature) to 25 °C (room temperature). For each temperature, every 15 minutes against the measurement time, a histogram of charges was made and fitted, and then the gain was calculated for each histogram. Figure 5.24 shows the distribution of gain for every 15 minutes at 15 °C.
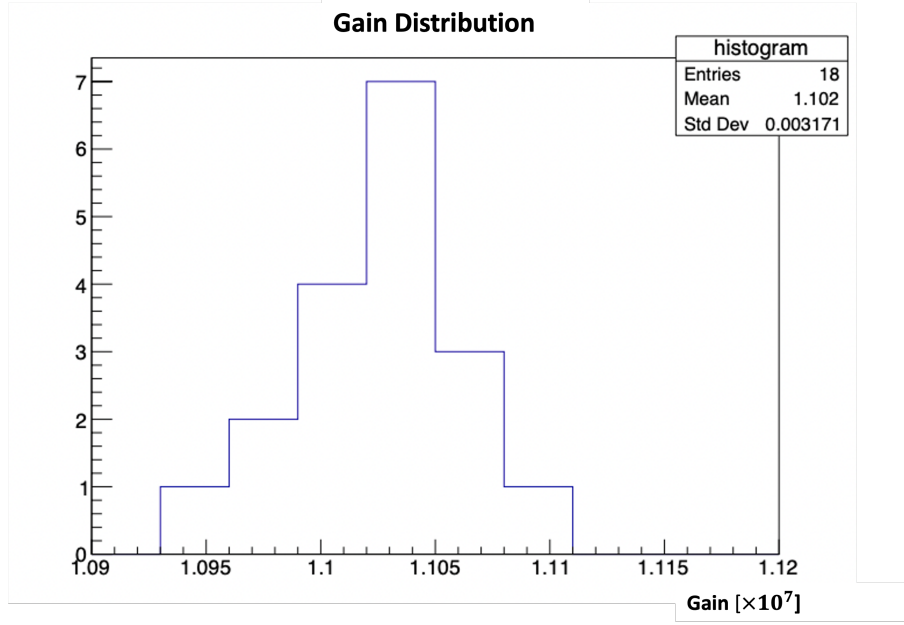
Figure 5.24. Gain distribution for every 15 minutes at 15 °C.

The mean of the obtained gains and the standard error of the mean (SEM) are plotted by temperature in Figure 5.25. The standard error of the mean is expressed using the standard deviation σ and the number of samples n as follows;

$$\mathrm{SEM} = \frac{\sigma}{\sqrt{n}} \tag{5.4}$$

Red points are those with correction by HV and black points are those without correction.
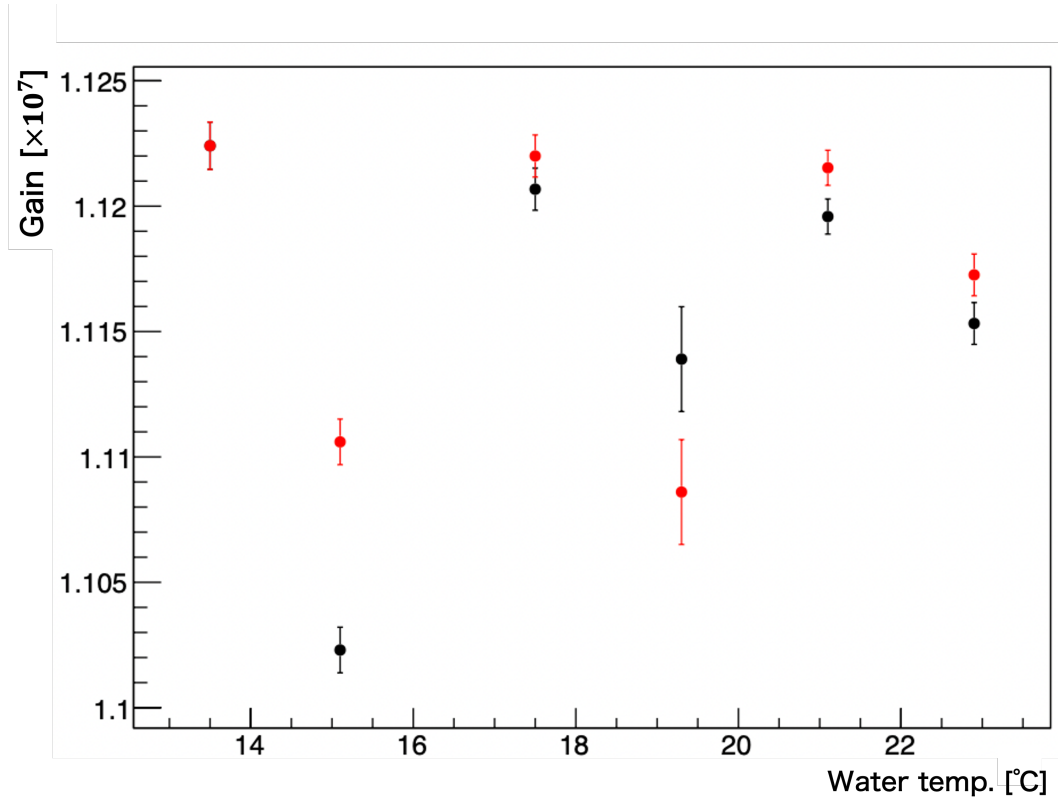
Figure 5.25. Measured gain at each water temperature. Red points are those with correction by HV and black points are those without correction.

Figure 5.26 shows each gain in Figure 5.25 divided by the mean and standard deviation of the gains for all temperatures.
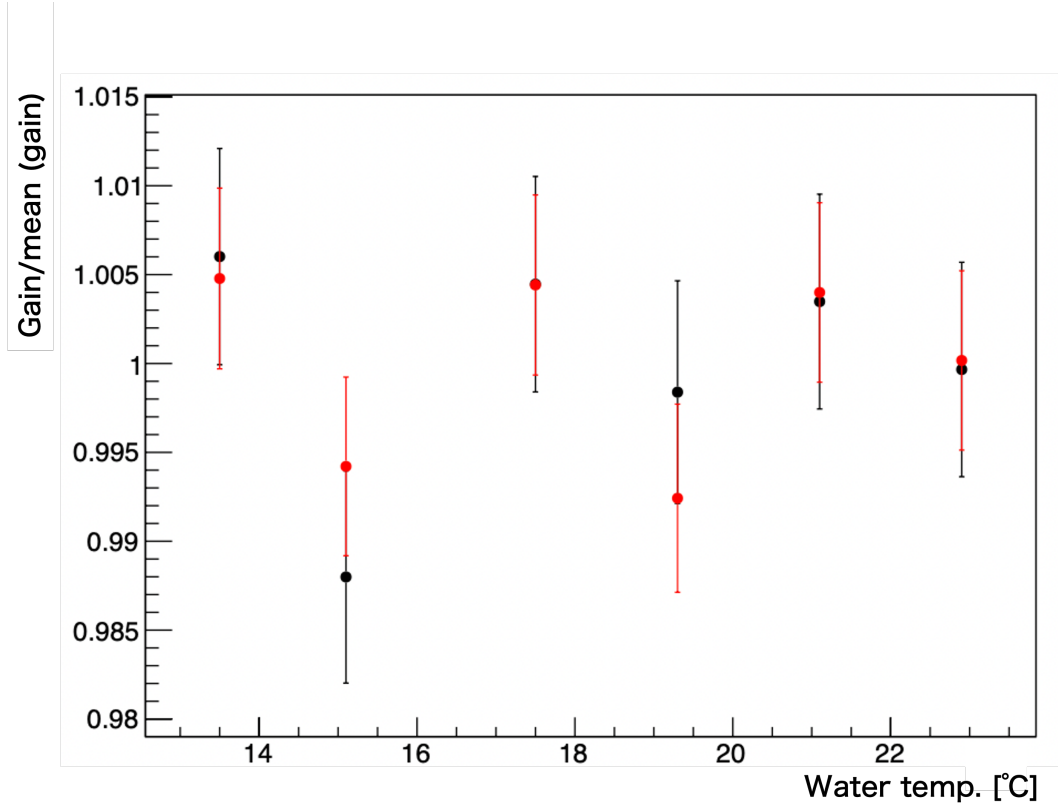
Figure 5.26. Measured gain divided by the mean.

From this result, it was found that the gain was constant within a range of $\pm 1\%$ between 13 °C and 23 °C.

5.4.2 Relative change in QE at different temperatures

This section discusses the relative changes in QE of 50-cm PMT at different temperatures. First, the "50-cm PMT light yield" at each temperature point is calculated, and then we define "relative QE" as their ratio.

The 50-cm PMT light yield is defined and derived as follows;

1. Assume that the SPE distribution created in the previous section follows a Poisson distribution. If the random variable X follows a Poisson distribution with the expectation of λ, the probability of k events in the same interval is expressed as follows;

$$P(X = k) = \frac{e^{-\lambda}\lambda^k}{k!} \tag{5.5}$$

2. When $k = 0$,

$$P(X = 0) = e^{-\lambda} \tag{5.6}$$

This $P(X = 0)$ is also expressed using the number of entries in the pedestal and the number of entries in the entire histogram as follows:

$$P(X = 0) = \frac{\text{Pedestal entries (red area in Figure 5.27)}}{\text{Entire histogram entries (blue area in Figure 5.27)}}$$
$$\stackrel{\text{def}}{=} p_0 \tag{5.7}$$
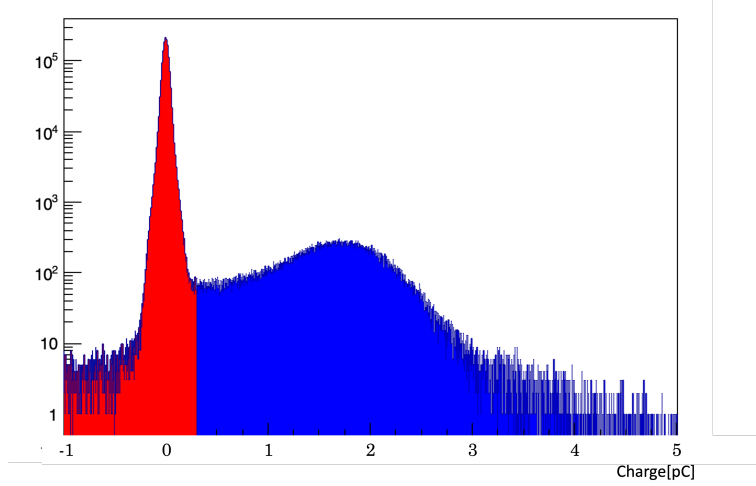
Figure 5.27. SPE distribution, blue area represents all entries, red area represents pedestal entries.

3. From above 1. and 2., the following can be obtained:

$$e^{-\lambda} = p_0$$
$$\lambda = -\log p_0 \tag{5.8}$$

We defined this λ as the 50-cm PMT light yield.

Figure 5.28 plots the relative QE for each water temperature, assuming that the laser light intensity had been constant. Here, relative QE is defined as the 50-cm PMT light yield at each water temperature divided by their average value. The SEM of the relative QE was about 0.1-0.2%, and the uncertainty of the monitored light yield was ±1%. Therefore, the error of each measurement is considered to be dominated by the variation of the monitor light yield, and this variations are plotted as the error.
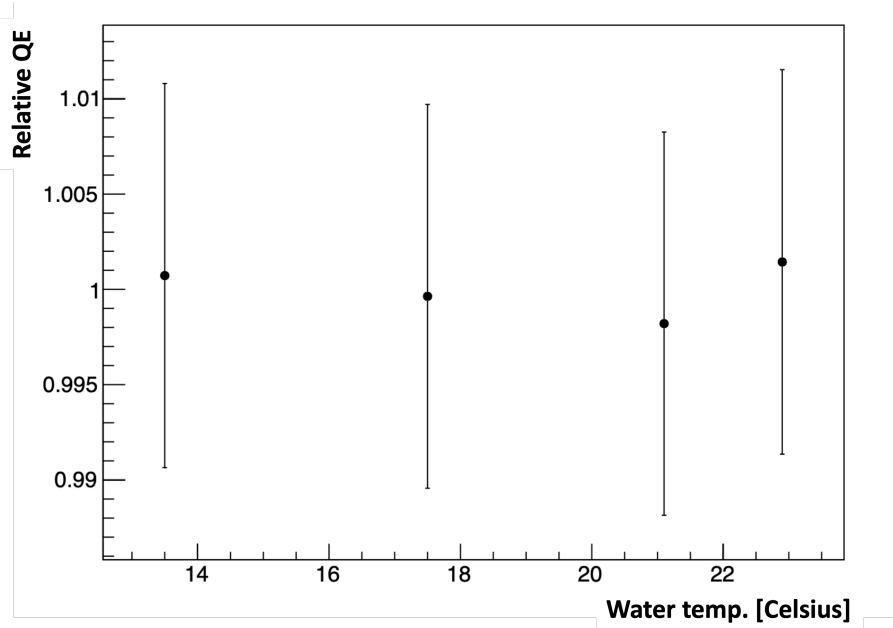
Figure 5.28. Relative change in QE at different temperatures.

From this result, we found that the relative QE is constant in this 13 - 23 °C range with an accuracy of ±1%.

5.4.3 Temperature dependence of dark rate

In the dark rate measurement, the baseline was first calculated as in the gain and monitor light yield. The ADC values between 100 - 850 ns are added together and averaged, which is defined as the baseline. Then, among the acquired waveforms, the number of waveforms that exceeded the "threshold" between 100 - 800 ns was counted. Most dark rate signals are approximately 1 photon level, and the threshold was set to 1/6 photon level. Since the output voltage corresponding to one photon of 50-cm PMT is roughly 6 mV, the threshold here was 1 mV (10 mV with amplifier). To verify whether this threshold is appropriate, a threshold scan was performed and the results are shown in Figure 5.30. This shows that the threshold value of 1 mV is reasonable.
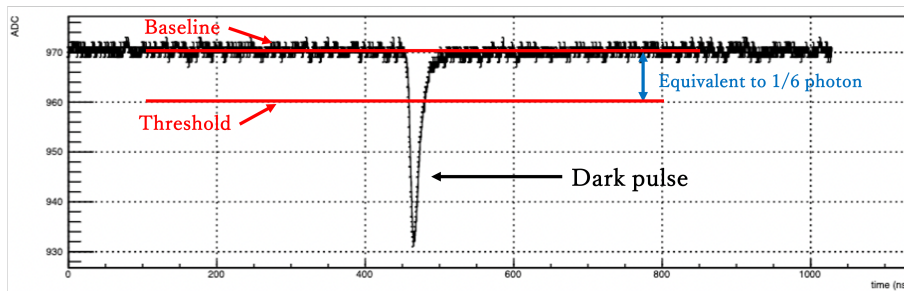
Figure 5.29. An example of dark pulse.
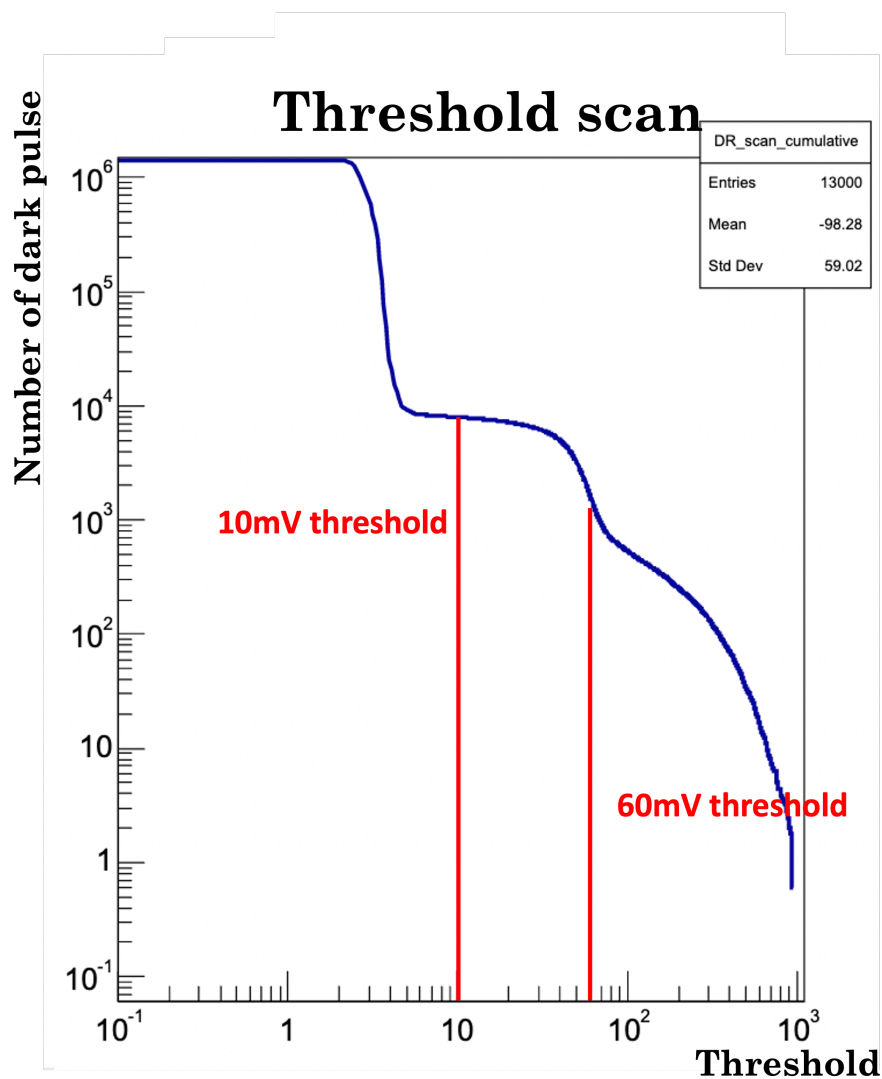
Figure 5.30. Threshold scan.

The dark rate results measured at 13, 17, 21, and 23 °C are shown in Figure 5.31. Each plot shows an average value every 30 minutes and its SEM. It was found that the dark rate fluctuation within this temperature range was within 5%.
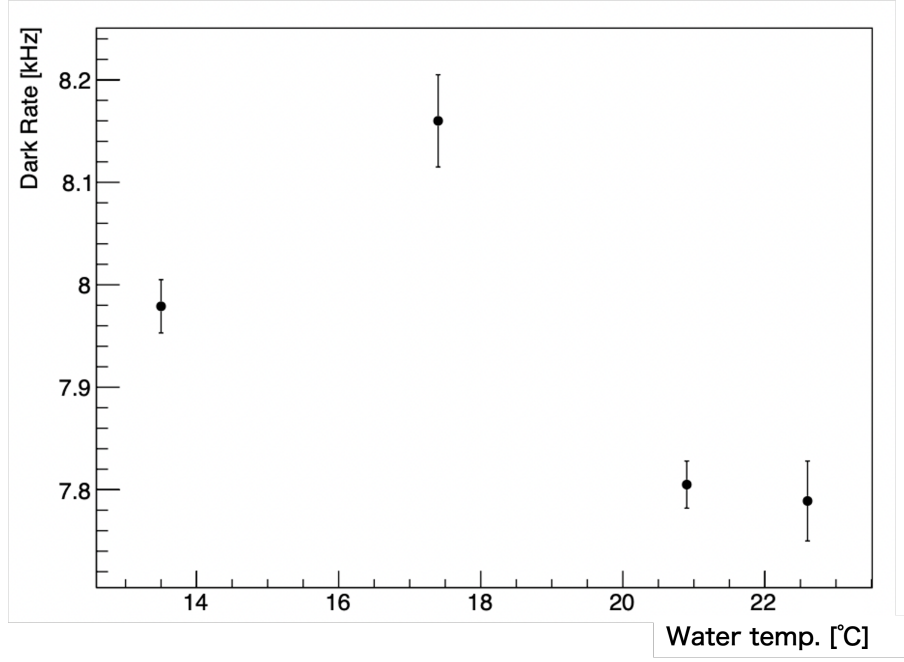
Figure 5.31. Measured dark rate at 13, 17, 21, and 23 °C.

Figure 5.32 shows the transition of the water temperature and dark rate when the water temperature was changed from 17 to 21 °C. The change in dark rate after the water temperature became constant was fitted using an exponential function;

$$f_{\text{dark rate fit}} = ae^{-\frac{(x-c)}{\tau}} + 7800 \tag{5.9}$$

where a and c are constants, τ represents the time constant, and the dark rate is assumed to be constant at 7800 Hz, and the constant term is set to 7800. The fit results show that the time constant is 9.9 hours. Therefore, it was found that it takes at least 10 hours for the dark rate to become constant, i.e., for the PMT glass temperature to become constant. Since the change in QE with temperature is considered to be mainly derived from the temperature change of the glass, this result is also applicable to the time required for QE stabilization.
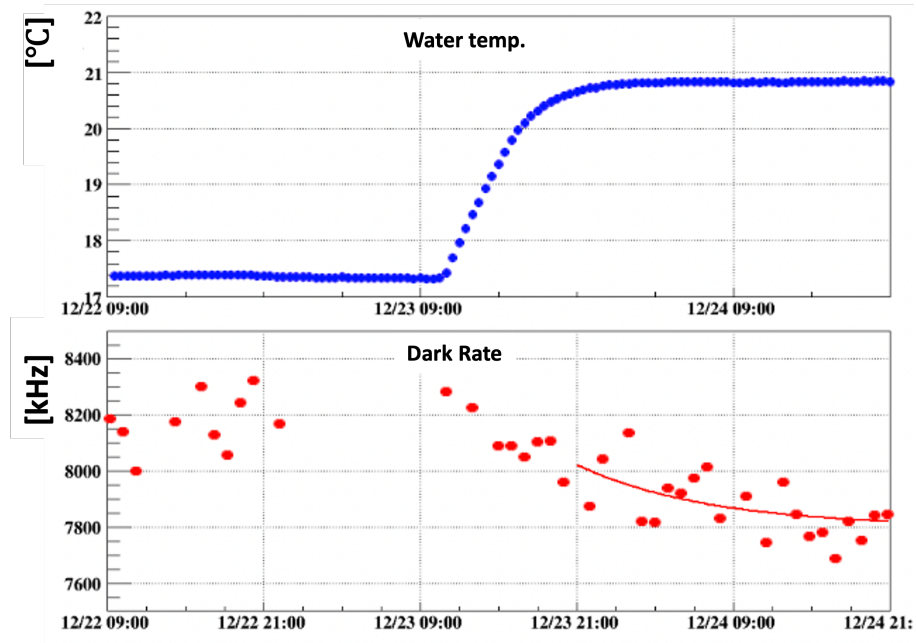
Figure 5.32. Change in water temperature and dark rate over time. The dark rate is fitted as an exponential function.

5.4.4 Gain in the air and in the water

Finally, the results of the gain measurements in air and in water are discussed. After the measurement in water at 23 °C, the water was drained from the tub and the gain was measured in the air. Because of the vacuum inside the PMT, heat conduction to the inside of the tube is poor. Therefore, the temperature of the dynode was assumed to be constant at 23 °C in the measurement within 4 hours after the water was drained. The results of the measurements are shown in Table 5.5.

Table 5.5. Comparison of gains in air and in water

	water	air
gain $[\times 10^7]$	1.134 ± 0.002	1.116 ± 0.004

A difference of about 1.4% was measured between gains in the air and in the water. The causes of this gap and countermeasures are discussed in Chapter 6.

5.4.5 Summary

We made the first measurement of the temperature dependence of the gain, relative QE, and dark rate of the R12860 PMT in water. In this measurement, it was confirmed that both the gain and relative QE were constant within a range of $\pm 1\%$. Regarding the dark rate, it was found that the dark rate fluctuation in 13 to 23 °C was within 5%, and the time constant of the dark rate change was about

57

10 hours. The gain in air and in air were also measured. In this measurement, a difference of 1.4% was observed between the two.

Chapter 6

Discussion

6.1 Impact on pre-calibration

For the Hyper-K detector calibration, it is required to be able to predict the performance of the 50 cm PMT at around 13 ℃ in water based on the pre-calibrated performance measured at room temperature in air. For this purpose, the temperature dependence of PMT performance must be evaluated, as well as the differences in PMT operation in water and air.

In this study, we constructed a setup that allows measurement in water and control of water temperature, and for the first time, measured the temperature dependence of the gain and relative QE of the 50-cm PMT and evaluated them with an accuracy of $\pm 1\%$. In addition, the temperature dependence of the dark rate was measured for the first time in water, and the time required for temperature stabilization of the glass was estimated from the change of the dark rate.

However, as an accuracy of better than 1% is required to achieve the physics goal of Hyper-K, this measurement also needs to be performed with even better accuracy. Besides, since this measurement was performed at only one light incident position, it is necessary to increase the number of incident positions and evaluate the position dependence of the 50-cm PMT performance. Evaluation of individual differences in PMTs and more detailed comparisons of the measurement in air and water are also important.

6.2 Future challenges

Ideas for improvements of this measurement and future prospects are listed below.

The first is to improve the measurement of relative QE. The error in the relative QE of this measurement originates from the measurement accuracy of the monitor light yield. More accurate measurement of the monitor light yield can be achieved by an improved temperature control of the measurement instruments. Looking at Figure 6.1, there appears to be a slight correlation between the laser's ambient temperature and the monitor light yield. To make measurements with better than 1% accuracy, it must be investigated whether the variation in monitor light yield originates from the laser source, the ADC, monitor PMT, or a combination of

these.
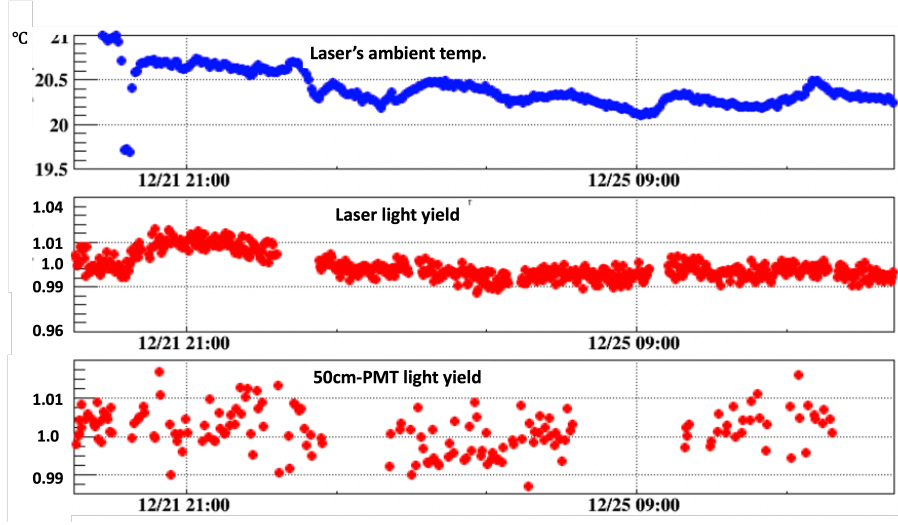
Figure 6.1. Measured laser's ambient temperature (top), monitor light yield (center), and 50cm-PMT light yield (bottom). The light yield is expressed as a ratio to the average of this range.

In addition, the time constant was estimated to be about 10 hours based on the change in dark rate, so a precise measurement of relative QE would require about 20 to 30 hours for QE stabilization.

The difference between gain in the air and the water also must be further investigated. There was a difference of 1.4% (more than 3σ) between the two. One of the factors that can differ between air and water is the surface potential of the photocathode, which is assumed to be 0 V for 50-cm PMT. If this value differs between air and water, it can affect the gain measurement. In our setup, using Equation 5.1, a 3.3 V difference between the two could result in a gain change of about 1.4%. Therefore, it is necessary to evaluate the surface potential of photocathode in water and air in the future.

Chapter 7

Summary

The Hyper-K experiment is a next-generation project that succeeds the Super-K experiment. With its large fiducial volume and approximately 20,000 newly developed high-performance 50-cm PMTs, Hyper-K aims to measure leptonic CP violation precisely, search for proton decay, observe astrophysical neutrinos and determine neutrino mass ordering. The achievement of these physics goals requires that the systematic error of the detectors be kept below 1%, which requires that all potential sources of systematic error, such as PMTs, electronics, and water, be calibrated with better than 1% accuracy before the observation begin. Among these calibrations, some 50-cm PMTs are measured their performance before their introduction into the tank to understand their response and to establish a method for evaluating their performance (pre-calibration). This pre-calibration is performed at a room temperature in air, whereas the actual operation of the 50-cm PMTs are in water at approximately 13 °C. Therefore, it is necessary to measure and evaluate in advance the effect of these environmental differences on the performance of the PMT.

In this study, a dark tub was used to construct a setup that allows underwater measurements and water temperature control. We made the first underwater measurement of the temperature dependence of gain, relative quantum efficiency (QE), and dark rate of the 50-cm PMT. The gain and the relative QE were measured to be constant with an accuracy of ±1% over the measured temperature range (13 - 23 °C). It was found that the dark rate fluctuation in this temperature range was within 5%, and the time constant of the dark rate change was about 10 hours. On the other hand, since Hyper-K requires to predict performance with better than 1% accuracy, more precise measurements are needed. In particular, the relative QE measurement was found to require a more temperature-controlled environment. The gains were measured both in air and in water and compared. As a result, there was a difference of about 1.4% between the two in this measurement. This also needs to be investigated further, for example by measuring the surface potential of the photocathode.

This study provides an important guideline for the pre-calibration measurement for the Hyper-Kamiokande experiment. Our results showed that the gain and relative QE of 50-cm PMT at 13 °C can be predicted with at least ±1% accuracy from those performances measured at a room temperature during the pre-calibration.

In addition, improvements for future measurements were discussed.

Acknowledgment

I would like to express my sincere gratitude to my supervisor, Prof. Yasuhiro Nakajima for giving me such an opportunity to conduct my research. I would also like to extend my gratitude to my fellow researcher, Yoshida-kun for his invaluable collaboration and dedication throughout this project. I am deeply grateful to Nishimura-san for lending me the dark tub for this measurement and to Patrick for lending me the water purification system.

I am thankful to the members of the Yokoyama-Nakajima group: Prof. Masashi Yokoyama, Prof. Kota Nakagiri, Daniel, Yoshimi, Eguchi-san, Kodama-san, Okinaga-kun, Kobayashi-kun, Arai-kun, Goto-kun, Mizuno-kun, Muro-kun, and Kono-san. In particular, Prof. Yokoyama and Prof. Nakagiri gave me a lot of support and helpful advice during my Master's course.

I appreciate the support and feedback from the members of the pre-calibration group, Ishitsuka-san, Yamaguchi-san, Izumiyama-san, Tsuchii-kun. Discussions with them were always helpful.

Finally, I would like to express my appreciation to my family for their consideration and kind support.

List of Figures

List of Tables

Bibliography

[1] K.Abe et al. "The Super-Kamiokande Experiment". In: *arXive* (2008). eprint: arXiv:0802.1041.

[2] Y. Fukuda et al. "Evidence for oscillation of atmospheric neutrinos." In: *Phys. Rev. Lett.* 81.1562 (1998). eprint: arXiv:hep-ex/9807003.

[3] K.Abe et al. "The Hyper-Kamiokande Experiment". In: *arXive* (2011). eprint: arXiv:1109.3262.

[4] C. L. Cowan et al. "Detection of the free neutrino: A Confirmation". In: *Science* 124 (1956). DOI: 10.1126/science.124.3212.103.

[5] S. P. Mikheyev and A. Yu. Smirnov. "Resonance Amplification of Oscillations in Matter and Spectroscopy of Solar Neutrinos". In: *Sov. J. Nucl. Phys.* 42 (1985), pp. 913–917.

[6] L. Wolfenstein. "Neutrino oscillations in matter". In: *Phys. Rev. D* 17 (9 1978), pp. 2369–2374. DOI: 10.1103/PhysRevD.17.2369. URL: https://link.aps.org/doi/10.1103/PhysRevD.17.2369.

[7] K.Abe et al. "Hyper-kamiokande design report". In: *arXiv* (2018). eprint: arXiv:1805.04163.

[8] Particle Data Group. "Review of Particle Physics". In: *Progress of Theoretical and Experimental Physics* 2022 (2022). URL: https://academic.oup.com/ptep/article-pdf/2020/8/083C01/34673722/ptaa104.pdf.

[9] Particle Data Group. "Measurements of neutrino oscillation parameters from the T2K experiment using 3.6×10^{21} protons on target". In: *arXiv* arXiv:2303.03222 (2023). URL: https://arxiv.org/abs/2303.03222.

[10] K. Abe et al. "Solar neutrino measurements using the full data period of Super-Kamiokande-IV". In: *arXiv* (2023). eprint: arXiv:2312.12907.

[11] *Hyper Kamiokande home page*. referenced 2023-12-25. URL: https://www-sk.icrr.u-tokyo.ac.jp/hk/about/outline/.

[12] S.Yoshida. "Performance evaluation of initial mass-produced 50 cm diameter photomultiplier tubes for Hyper-Kamiokande". Master Thesis, University of Tokyo. 2023. URL: https://www-sk.icrr.u-tokyo.ac.jp/hk/doc/thesis/yoshida_mthesis.pdf.

[13] Matthew Malek. "Hyper-Kamiokande: Status and Plans". The University of Sheffield. Reported at "30th International Symposium on Lepton Photon Interactions at High Energies". 2022. URL: https://indico.cern.ch/event/949705/contributions/4555521/attachments/2371006/4049381/Malek-20220111-LeptonPhoton.pdf.

[14] Laura-Iuliana Munteanu. "Towards the measurement of CP violation in neutrino oscillations with the T2K experiment". In: *NNT:2021UPASP049* (2021). URL: https://artxiker.ccsd.cnrs.fr/CEA-UPSAY/tel-03474937v1.

[15] Takatomi Yano. "Solar neutrino physics at Hyper-Kamiokande". In: *36th International Cosmic Ray Conference* 358 (2019). DOI: https://doi.org/10.22323/1.358.1037. URL: https://pos.sissa.it/358/1037/pdf.

[16] Y.Nishimura. " ハイパーカミオカンデの大口径光検出器開発 ". In: 高エネルギーニュース. Vol. 41. 2021.

[17] Xia Junjie. "Upgrade and Calibration of Super-Kamiokande's Inner Photodetectors". Master Thesis, University of Tokyo. 2019. URL: https://www-sk.icrr.u-tokyo.ac.jp/sk/_pdf/articles/MasterThesis-XIA_JUNJIE-35176375.pdf.

[18] K. Abe et al. "Calibration of the Super-Kamiokande Detector". In: *arXiv* (2013). eprint: arXiv:1307.0162v2.

[19] S. Shima. "Study of Super-Kamiokande detector calibration using cosmogenic neutron capture on Gadolinium". Master Thesis, University of Tokyo. 2023. URL: https://www-sk.icrr.u-tokyo.ac.jp/sk/_pdf/articles/2023/mth2023_shima.pdf.

[20] S. Sakai. スーパーカミオカンデにおける検出器較正の研究. Master Thesis, Okayama University. 2021. URL: https://www-sk.icrr.u-tokyo.ac.jp/sk/_pdf/articles/2021/Master_thesis_Sakai_final.pdf.

[21] CAEN. *Technical Information Manual*. Nov. 2012. URL: https://www.caen.it/products/dt5761/.

[22] CAEN. *WaveDump UserManual rev20*. Jan. 2023. URL: https://www.caen.it/products/caen-wavedump/.